TEXEL: A NEUROMORPHIC PROCESSOR WITH ON-CHIP LEARNING FOR BEYOND-CMOS DEVICE INTEGRATION

Hugh Greatorex[1,2,*]   **Ole Richter**[1,2]   **Michele Mastella**[1,2]   **Madison Cotteret**[1,2,3]

Philipp Klein[1,2]   **Maxime Fabre**[1,2,4]   **Arianna Rubino**[5]   **Willian Soares Girão**[1,2]

Junren Chen[5]   **Martin Ziegler**[3]   **Laura Bégon-Lours**[6]   **Giacomo Indiveri**[5]

Elisabetta Chicca[1,2,*]

ABSTRACT

Recent advances in memory technologies, devices and materials have shown great potential for integration into neuromorphic electronic systems. However, a significant gap remains between the development of these materials and the realization of large-scale, fully functional systems. One key challenge is determining which devices and materials are best suited for specific functions and how they can be paired with CMOS circuitry. To address this, we introduce TEXEL, a mixed-signal neuromorphic architecture designed to explore the integration of on-chip learning circuits and novel two- and three-terminal devices. TEXEL serves as an accessible platform to bridge the gap between CMOS-based neuromorphic computation and the latest advancements in emerging devices. In this paper, we demonstrate the readiness of TEXEL for device integration through comprehensive chip measurements and simulations. TEXEL provides a practical system for testing bio-inspired learning algorithms alongside emerging devices, establishing a tangible link between brain-inspired computation and cutting-edge device research.

[1]Bio-Inspired Circuits and Systems (BICS) Lab, Zernike Institute for Advanced Materials, University of Groningen, Netherlands.
[2]Groningen Cognitive Systems and Materials Center (CogniGron), University of Groningen, Netherlands.
[3]Micro- and Nanoelectronic Systems (MNES), Technische Universität Ilmenau, Germany.
[4]Forschungszentrum Jülich, Germany.
[5]Institute of Neuroinformatics, University of Zürich and ETH Zürich, Switzerland.
[6]D-ITET Integrated Systems Laboratory, ETH Zürich, Zürich, Switzerland.
[*]Corresponding authors {h.r.greatorex, e.chicca}@rug.nl

1 Introduction

The unsustainable energy requirements of current deep learning algorithms have promoted research into novel computing architectures and technologies. Some of these efforts are aimed at emulating the computational principles of biological intelligence to enhance efficiency and processing capabilities. In this regard, the development of neuromorphic computing architectures has seen substantial growth [1–7]. In particular, neuromorphic systems using hybrid CMOS-memristive circuits offer a promising direction for low-power, highly compact In-Memory Computing (IMC) solutions [8, 9]. Memristive technologies encompass a wide range of novel electronic materials and devices that possess inherent memory and reprogrammability through state-dependent, and possibly non-volatile, resistance modulation [10].

When integrated in CMOS Spiking Neural Network (SNN) chips, hybrid neuromorphic/memristive circuits can exploit the physics of the devices and their intrinsic dynamics to carry out low-power computations that extend the basic advantages of conventional IMC dense crossbar array architectures [11]. Conventional IMC neural network designs, which use either digital Static Random Access Memory (SRAM) or memristive crossbars, aim to maximize peak throughput and area efficiency [12–14]. In contrast, mixed-signal neuromorphic architectures seek to reduce overall power consumption, especially in edge computing applications like bio-signal processing or environmental monitoring, which involve slowly varying signals [15]. Recent research has focused on brain-inspired neural mechanisms to implement efficient neural networks targeting edge-computing applications [16, 17]. These types of architectures implement SNNs, where the spikes are digital events communicated via asynchronous digital logic. Both the analog circuits implementing the slow neural and synaptic dynamics as well as the asynchronous digital circuits implementing the event-based routing and network (re)programmability, enable ultra-low power computation. Typically, the analog circuits used in these neuromorphic platforms rely on the subthreshold analog transistor regime [18] to emulate neuron-like dynamics for a further reduction in energy cost [6, 19, 20].

By exploiting the physics of the devices, this approach has led to the development of a diverse array of circuits that implement computational models of synaptic plasticity [21]. Synaptic plasticity is the ability of synapses to be potentiated or depressed in a volatile (short-term plasticity) or non-volatile manner (long-term plasticity) [22]. Although pure CMOS hardware implementations of local synaptic plasticity rules have been shown to express complex and powerful computational properties [2, 23, 24], they require substantial silicon real-estate to store the synaptic weights. Addressing this issue has traditionally involved a common strategy: driving the weight to a stable value for storage. The use of bistable plastic synapses originates from some of the first developments of full-scale neuromorphic systems [24, 25] mimicking biological synapses

which inherently have limited bit precision [26, 27]. Other works propose to update the weights directly within a digital memory [2, 28], thus facilitating a long-term storage, but they often require a continuous power supply to maintain the memory. Combining the mixed-signal neuromorphic engineering approach with the integration of memristive devices, would simultaneously enable the exploration of additional computational strategies, such as intrinsic stochasticity and state-dependence, as well as provide a compact and non-volatile storage option for maintaining weight values during power-cycles.

Recent efforts have thus initiated the exploration of integrating memristive devices with CMOS neuromorphic systems, aiming to leverage the synergy of both technologies [29–35]. A majority of these efforts have focused on complementing memristive crossbar arrays with neuromorphic peripheral circuitry to handle the generation of output spikes and the computation of learning signals [30–32]. Synaptic weights in these systems are realized by the resistance states of memristive devices in a crossbar array. To modify these weights, suitable read and write processes must be developed, which can compromise the systems' ability to perform IMC. On the other hand, few works explore the possibility of implementing IMC synaptic plasticity, with learning directly occurring at each synaptic device. In [33] the authors proposed a differential three-terminal device interface to achieve more flexible device access for online learning while [34] and [35] proposed the exploitation of memristive device dynamics to implement in-memory plasticity directly in the crossbar. Although these approaches have been explored, they have been limited to simulations of a few circuit elements with restricted learning flexibility.

In this work, we introduce TEXEL, a fully fabricated chip combining the operational efficiencies of memristive devices with the spike-based approach of neuromorphic systems. The chip exploits the analog subthreshold CMOS regime and event-based computation to implement ultra-low power spiking neurons and plastic synapses with tunable always-on trace-based local learning functionality. TEXEL incorporates a novel Back-End Of Line (BEOL) device-agnostic differential synaptic interface, enabling the integration of a wide range of two- and three-terminal memristive devices across all 9K plastic synapses atop the CMOS chip. This design makes TEXEL a versatile research platform for large-scale BEOL device integration in neuromorphic systems. While devices are yet to be integrated, TEXEL represents, to the best of our knowledge, the first memristor-based large-scale neuromorphic chip with on-chip learning that is fully-fabricated. It exploits the synergies of IMC and spiking neural networks to present a concrete step towards the following key developments for such systems:

1. Exploiting the capability of memristive materials and devices to facilitate the implementation and consolidation of on-chip synaptic plasticity.
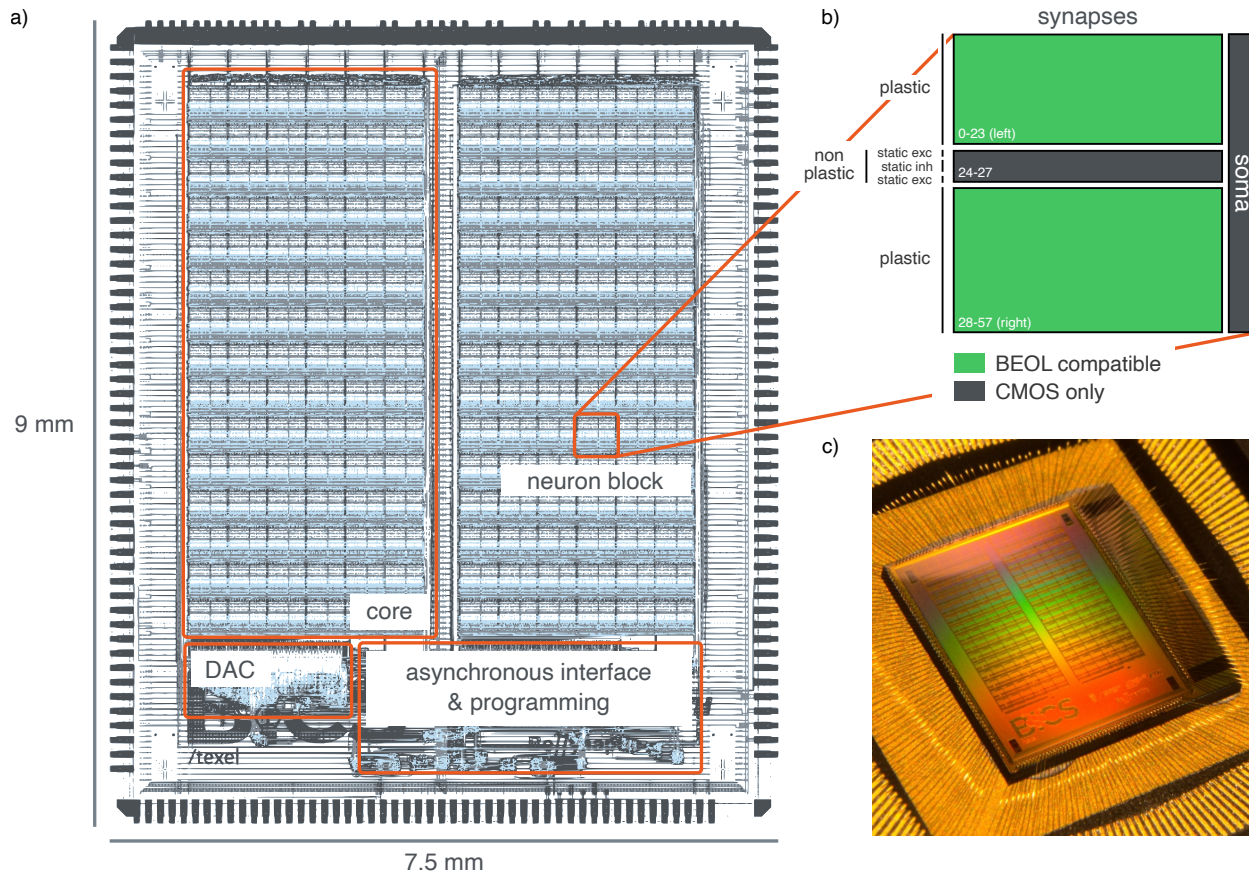
Fig. 1: **The fabricated TEXEL chip. a)** Footprint of the chip, indicating the location of the architectural blocks. **b)** The neuron block footprint, indicating the synaptic fan-in of the soma within the block. The location of the plastic and non-plastic synapses are shown with excitatory (exc) and inhibitory (inh) types. The plastic synapses contain the contacts and interface circuitry for BEOL integration of memristive devices. **c)** A photograph of the $9\,\mathrm{mm} \times 7.5\,\mathrm{mm}$ die, fabricated using the XFAB $180\,\mathrm{nm}$ process.

2. Providing a platform to explore the large-scale BEOL integration of memristive materials and devices with an SNN processor.

Here, we present the architectural innovations and learning mechanisms of the TEXEL chip, highlighting its impact on the ongoing development of neuromorphic computing and the pursuit of beyond-CMOS device integration. Through comparisons with other existing full-scale neuromorphic chips, we highlight TEXEL's unique contributions and envisage its role in advancing the frontier of computing toward more efficient, brain-inspired paradigms.

2 Results

Silicon measurements that validate the functionality of the TEXEL chip (Fig. 1) and are outlined in the following sections. Experiments using the on-chip learning circuits demonstrate the emergent phenomena of Spike Timing Dependent Plasticity (STDP) [36] and Spike-Rate-Dependent Plasticity (SRDP) [37]. The functionality of memristive

device read-write circuits are verified experimentally, and the operation of the interfacing circuits is demonstrated with post-layout simulations, which define the parameter range of memristive devices aiming for compatibility with TEXEL. Power consumption measurements provide a detailed breakdown of the contribution of each circuit block, exemplifying the inherent power efficiency advantages of subthreshold analog circuitry and the event-driven paradigm.

2.1 Neural Circuits

We measured the activation of the silicon neuron circuits to assess their transfer function and operating regimes. A Direct Current (DC) input was applied and systematically increased across all neurons while their spike rate was recorded (Fig. 2a). The resultant Frequency vs. Current (FI) curve shows both the aggregate mean response for each core as well as the individual activation profiles of all neurons. The discernible core-specific disparity is attributable to mismatch in the biasing circuitry. The dis-

persion in the FI curve of each neuron stems from inherent variations in individual neuron circuits. While device mismatch variability can be reduced by including calibration procedures for each element [2], we chose to minimize it, through judicious analog circuit design techniques, and keep it, as it can be exploited for example in learning [38].

We conducted validation measurements of the adaptive characteristics embedded in the circuitry of each neuron. The response of the membrane potential to a DC step input was measured, as well as the timing of output spikes (Fig. 2b). These observations reveal the expected temporal pattern in the neuron's instantaneous spike rate, characterized by an initial peak followed by a gradual decay towards a stable state (Fig. 2c). Figure 2d shows an instance in which a neuron is stimulated by a Poisson spike train through its static excitatory synapses. The plastic synapses located within each neuron block are quantized to a binary value which is translated into an analog bias representing high and low synaptic efficacy. The on-chip weight matrix, encoding the state of all plastic synapses, can be read-out post learning and also programmed for inference (see Supplementary Fig. S4).

2.2 Learning Circuits

The on-chip plasticity was implemented using mixed-signal circuitry embedded within each plastic synapse. This circuitry emulates the Bistable Calcium-based Local Learning (BCaLL) rule [39], which combines STDP for low activity with Hebbian changes [40] at high activity. In this model, synaptic updates are driven by pre- and postsynaptic calcium traces representing neuronal activity. A secondary postsynaptic trace (Ca^{2+}) with a slower time constant acts as a plasticity gating mechanism, ensuring weight updates occur only within specific firing rate ranges. The learning rule imposes a bistable analog internal weight (V_w) to help mitigate catastrophic forgetting in binary synapses [37, 41–43], stabilizing synaptic states using accumulated updates and bistability circuitry.

Figure 3a shows measurements of a plastic synapse undergoing short-term depression. Pre-trace integration of presynaptic spikes maintains a decaying record of presynaptic activity, but without postsynaptic activity, the synaptic weight remains unchanged. When postsynaptic spikes occur, plasticity becomes apparent, and if the post-trace crosses it's lower threshold, depression is triggered. The synaptic weight experiences short-term depression but stabilizes to the high state due to bistability circuitry.

We conducted in-silico experiments to characterize STDP of the learning circuitry (Figs. 3b, 3c). The synaptic weight changes (Δw) were measured by systematically varying pre- and postsynaptic spike timings. Adjusting the biasing parameters allowed for on-chip configuration of STDP curves, enabling the introduction of depressive regions for positive pre-post pairings. Additionally, SRDP was measured by varying pre- and postsynaptic Poisson spike rates. A probability map (Fig. 3d) of synaptic weight changes

demonstrates that under conditions of high presynaptic and postsynaptic activity, the likelihood of the synapse settling into a potentiated (high) state increases. In contrast, when activity levels are lower, the synapse is more likely to undergo depression, favoring the low-weight state. This data highlights the sensitivity of the learning circuitry to the frequency and timing of local spiking activity.

2.3 Memristive Device Interfacing Circuits

Each plastic synapse on TEXEL (Fig. 1b) can be enabled to utilize a pair of memristive devices to store a binary weight using a differential device configuration [44, 45]. When the chip is programmed to enable device operation, at the time of a presynaptic spike, the synaptic weight is read using a differential normalizer circuit [33]. To demonstrate the operation of the normalizer circuitry we performed extensive Spectre post-layout simulations over a range of memristive device parameters, namely: conductance, capacitance and on-off ratio. The memristive devices were modelled as parallel RC circuits. Figure 4a shows how the differential device setup, consisting of a "positive" and "negative" device, is able to store the binary synaptic weight. In the case where the resistance of the positive device is lower than that of the negative device, the current sourced through the positive device, I_{pos}, during a read pulse (presynaptic spike) is greater than the current sourced through the negative device, I_{neg}. In this scenario the normalizer circuit transmits a current, I_{norm}, proportional to the biasing of the normalizer circuit, norm_bias. For these simulations the current was normalised to $200\,\text{nA}$ (norm_bias) and passed into a Differential Pair Integrator (DPI) synapse [46] to elicit a postsynaptic current, I_{syn}. In the alternative case, when the differential synapse is programmed to represent a low weight, the positive device resistance is greater than the negative device resistance. Therefore $I_{neg} > I_{pos}$ and the normalizer circuit does not convey a current. Figure 4b presents post-layout simulation results showing how I_{norm} varies with the ratio of the positive and negative device conductance. When the ratio is < 1, I_{norm} is zero, conversely when the ratio is > 1, I_{norm} is large enough to elicit a postsynaptic current. For large ratios between the positive and negative devices, translating to a large on-off ratio, the differential synapse and normalizer circuit is able to source a current that is closer to norm_bias.

2.4 Memristive Device Requirements

To quantify the compatibility of TEXEL with co-integrated memristive devices we performed extensive Spectre post-layout simulations of the CMOS interface circuitry with realistic device characteristics, over several orders of magnitude. We parameterised all simulations using a fixed read voltage pulse width of $500\,\mu\text{s}$ and a norm_bias of $200\,\text{nA}$, however these can be varied using the on-chip programming and biasing. Figure 4c shows a heat-map of a 2D logarithmic device characteristic sweep during which the on-off conductivity ratio of the device was varied with
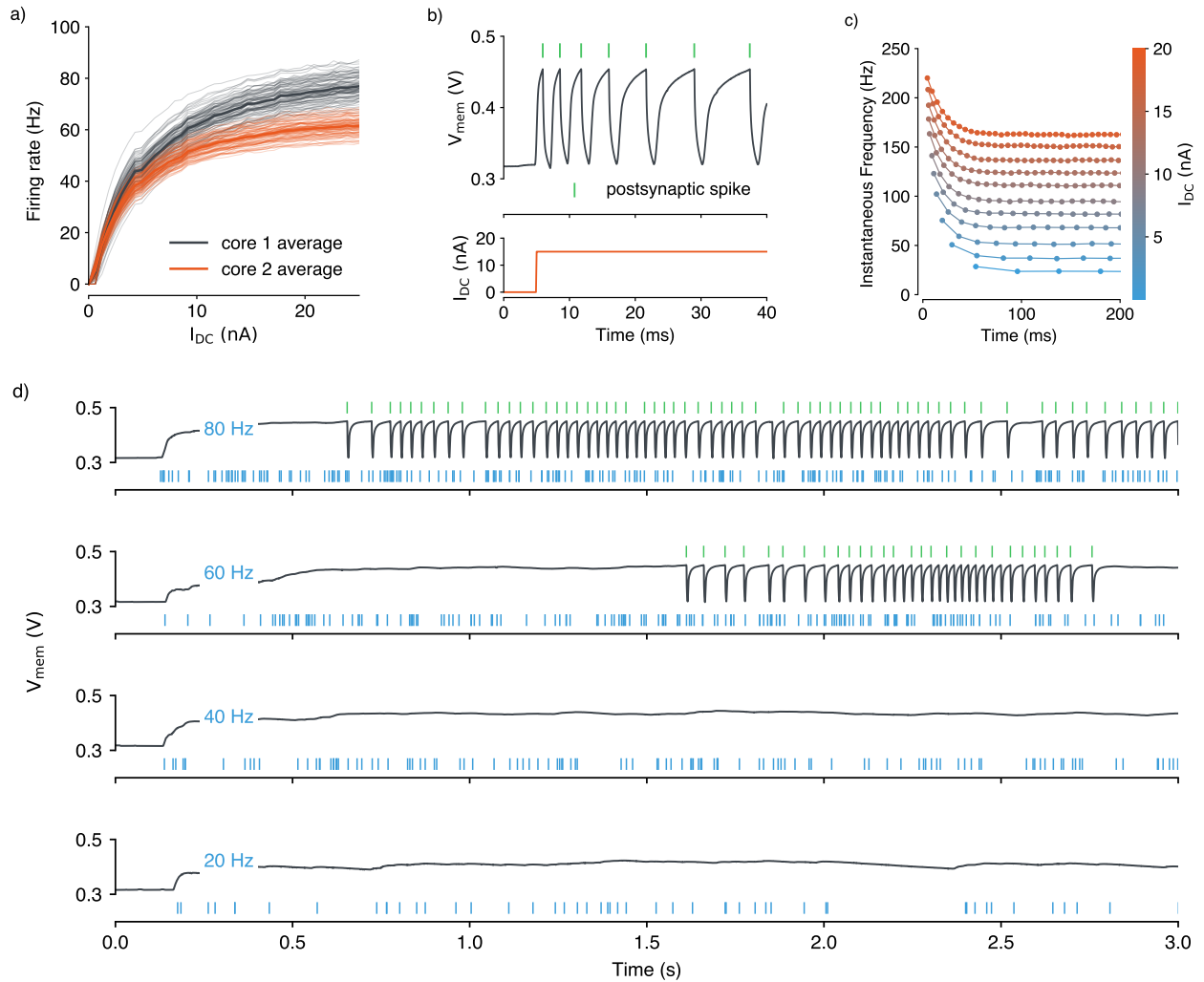
Fig. 2: **Measurements of the neuron circuitry on the TEXEL chip. a)** The measured firing rates of all neurons on TEXEL in response to a constant DC input current. **b)** Measurement of the membrane potential of a single neuron in response to a DC step input. The neuron's adaptation characteristic is evident as its firing rate begins high and gradually diminishes to attain a steady state. **c)** Measurements of the variations in the instantaneous firing rate and timing of output spikes in relation to the magnitude of DC injected into the soma. **d)** The recorded membrane potential response of a neuron receiving presynaptic Poisson input at the static excitatory synapses. Below, in blue, is the presynaptic spike train, while above, in green, the postsynaptic spikes indicate the neuron's spiking activity.
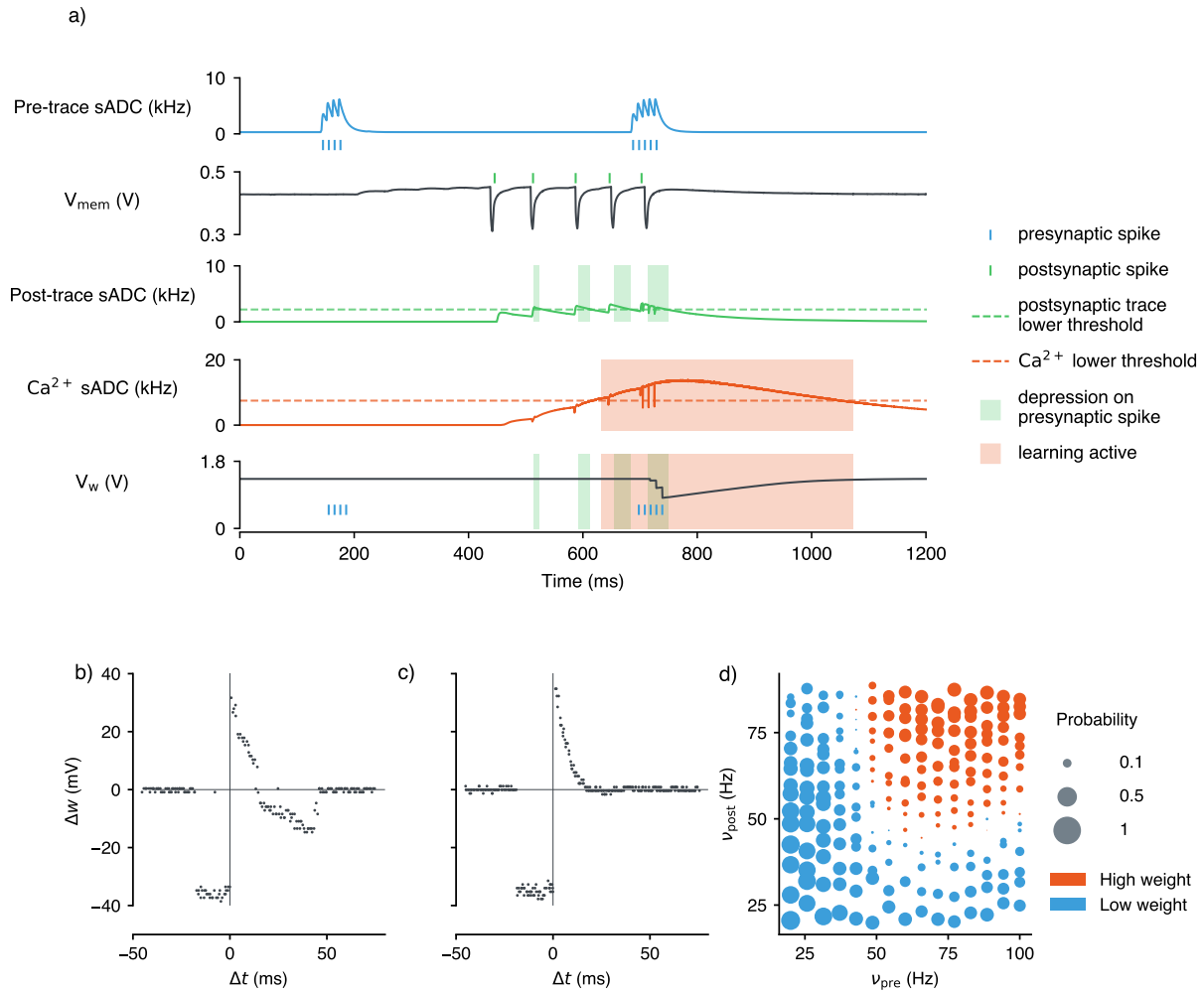
Fig. 3: **Silicon measurements of a single plastic synapse and its neuron, demonstrating local synaptic plasticity (complementary to Fig. 6b). a)** A presynaptic spike train induces a current (blue) read by the spiking Analog Digital Converter (sADC), while simultaneous stimulation with an Excitatory Post Synaptic Current (EPSC) triggers postsynaptic spiking (green). Shaded regions indicate when the post-trace exceeds the lower threshold, reflecting short-term memory. The Ca^{2+} trace (orange) accumulates postsynaptic activity, showing plasticity when above its threshold. **b)** STDP measurements assess the impact pre- and postsynaptic spike timing, $\Delta t = \mathrm{pre} - \mathrm{post}$, on the analog weight of the synapse (w). **c)** This STDP curve demonstrates modulation of potentiation and depression through analog biasing. **d)** SRDP results show the probability of the synapse having high or low weight based on pre- and postsynaptic firing rates (ν_{pre} and ν_{post}).
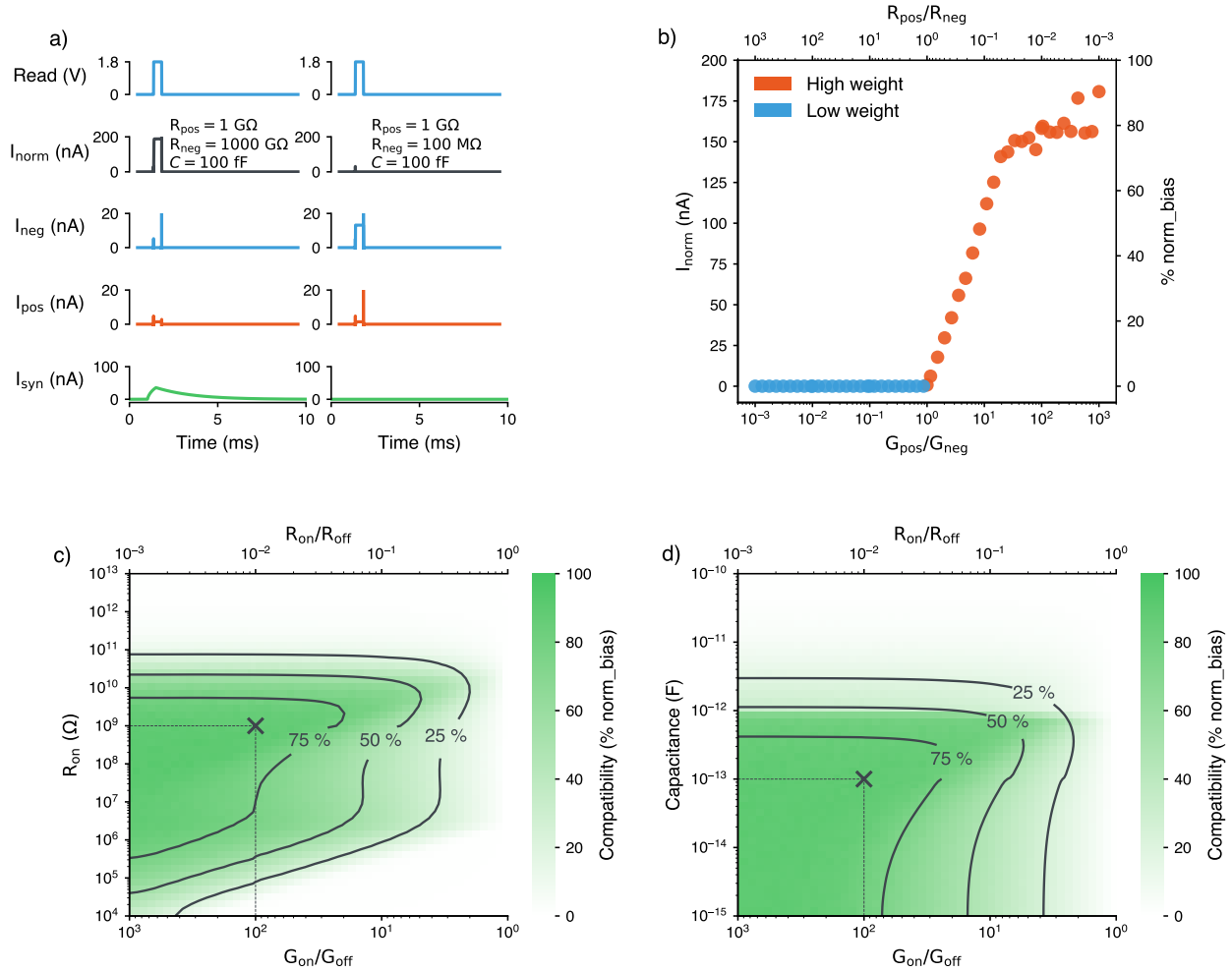
Fig. 4: **Spectre post-layout simulations of the read protocol for the differential normalizer synapse on TEXEL. a)** A read pulse with a width of $500\,\mu s$ activates the normalizer circuit, sourcing I_{neg} and I_{pos}. The circuit outputs a non-zero current, I_{norm}, if $I_{pos} > I_{neg}$, which is integrated by a DPI synapse, resulting in a current I_{syn} sent to the neuron. The left panel shows high weight storage ($R_{pos} < R_{neg}$), eliciting a response, while the right panel shows low weight storage ($R_{neg} < R_{pos}$), where no current is integrated. **b)** With $R_{pos} = 1\,G\Omega$, device capacitance of $C = 100\,fF$, and a read pulse width of $500\,\mu s$, the relative resistances of both devices are varied by sweeping R_{neg}. The average output current of the normalizer circuit is measured as a % of norm_bias, showing non-zero current when the positive device's conductance exceeds that of the negative device. **c)** Simulations explore device characteristics' impact on compatibility with TEXEL. The cross ($\times$) represents a device with $C = 100\,fF$, $G_{on}/G_{off} = 100$, $R_{on} = 1\,G\Omega$, and a read pulse width of $500\,\mu s$. Heatmaps indicate average current from the normalizer as a percentage of norm_bias. **d)** A sweep of the device's capacitance versus its on/off ratio is shown with R_{on} fixed at $1\,G\Omega$.

the on-resistance. This heat-map shows the percentage of the norm_bias of the normalizer circuit that was sourced during a read voltage pulse that was sent to the differential device synapse when storing a high weight. This is used as the metric determining whether a memristive device will operate as expected when integrated with the TEXEL chip and defines the "compatibility". Similarly, we performed simulations varying the on-off conductivity ratio and capacitance of the device (Fig. 4d), here the same metric of compatibility is used. This is an additional memristive device constraint that must be satisfied to ensure successful integration with CMOS and one that is often overlooked. Table 1 presents the integration specifications derived from the aforementioned simulations, operating voltages and circuit footprints.

2.5 Power Measurements

We conducted extensive power measurements on the TEXEL chip using a femtoampere Source Measurement Unit (SMU) to assess its power distribution across operations for the analog and digital power sources. Figure 5a and 5c show how the dynamic power consumption varies with the global spike rate of the chip, this was modulated by increasing the DC input bias for all neurons. The total dynamic power consumption is divided into the contributions of the isolated digital, analog and padframe power supplies. The energy per spike was also calculated for varying spiking rates (Fig 5b, Fig 5d). Figure 5e and 5f show the same power contribution breakdown for synaptic operations with the energy required per operation. This experiment was performed by increasing the input spike rate over the Address Event Representation (AER) bus, randomly addressing all synapses on the chip, over both cores. Figure 5g shows the breakdown of the static power consumption of the chip, measured at $27.4\,\mu\text{W}$.

3 Discussion

Recent advancements have produced only a few successfully co-integrated large-scale memristor-CMOS neuromorphic systems [47–51], with most relying on foundry assistance [48–51]. This lack of co-integration is a key challenge in advancing memristor-CMOS systems, emphasizing the importance of wafer-level integration platforms to bridge the gap with CMOS technology and to progress neuromorphic chip development.

In this work, we introduced TEXEL, an SNN processor with on-chip learning circuits capable of interfacing with a large range of memristive device operation requirements (Table. 1). TEXEL functions in both full-CMOS and device-integrated modes, offering a versatile platform to explore emerging memristive technologies within the context of a spiking neuromorphic system. The platform supports a wide range of device interfacing options, including read-write pulse widths from $10\,\text{ns}$ to $100\,\text{ms}$, continuous read and pre-charge

modes (see Supplementary Section A.4), and high-voltage compatibility up to $5\,\text{V}$. It can interface with either two-terminal devices or three-terminal devices such as Ferroelectric Field Effect Transistors (FeFETs) [52, 53].

The chip also provides a crucial substrate for testing yield and endurance - key factors in device fabrication at scale. When incorporated into SNN systems, these properties can be evaluated in real-world learning tasks, while on-chip learning algorithms enable continuous performance characterization through repeated weight updates. This iterative process provides valuable insights into the ability of algorithms to mitigate drift in device characteristics and maintain performance over time. While TEXEL's broad compatibility with Non-Volatile Memory (NVM) devices provides flexibility, it also introduces significant area overhead (see Table 2 and Supplementary Fig. S3). Future iterations, once a specific NVM technology is chosen, should aim to optimize both density and performance. TEXEL prioritizes flexibility over efficiency by supporting multiple device debug modes and allowing operation without devices for CMOS circuit verification. Nonetheless, the ability to monitor a wide range of signals remains essential for benchmarking and debugging hybrid memristor-CMOS systems (see Supplementary Table 1).

Broadly, the integration of memristive devices and materials with CMOS extends beyond storing and reading synaptic weights; they can also be incorporated into neuron [54] and learning circuits [55], enhancing characteristics such as time constants. Moreover, these emerging devices and materials have shown significant promise in sensory applications [56, 57], rendering them particularly appealing for integration into sensory front ends that can be interfaced with always-on neuromorphic chips. They have also been shown to facilitate the implementation of additional network features, such as synaptic delays [29] and specific network topologies [58], further enhancing the richness and versatility of neuromorphic systems. Collectively, these capabilities position memristive device technology as a key component in the development of efficient and adaptable electronic architectures. With its flexibility, TEXEL serves as a foundational tool for expediting the realization of memristor-CMOS systems, paving the way for scalable, state-of-the-art spiking neural network chips that can effectively leverage emerging device technologies.

4 Methods

4.1 Chip Architecture

With 2 cores of 90 neuron blocks, TEXEL hosts 180 neurons each with 58 complex synapses (Fig. 1b). The chip's digital periphery operates asynchronously, utilizing handshake protocols between functional blocks [59]. Robustness was tested through extensive testing for variable switching delays, eliminating the reliance on specific timing constraints. Spike I/O and register operations share an asynchronous pipeline tailored for AER. Demux circuits route incoming packets to either the spike decoder

	Read Voltage (V)	Set Voltage (V)	Reset Voltage (V)	Area (μm^2)
Min.	0	-5	-5	-
Max.	5	5	5	114

	Total Capacitance (pF)	Capacitance/Area (F/cm^2)	R_{on} (GΩ)	G_{on}/G_{off} -
Min.	-	-	-	10
Max.	10	8.8×10^{-7}	10	-

Table 1: **TEXEL memristive device compatibility requirements for integration.** Entries in the second row are derived from post-layout simulations (Fig. 4), 50% is taken as a confidence threshold for compatibility.

Chip	TEXEL [this work]	ISSCC'20 [48]	ISCAS'23 [50]	NeuRRAM [49]
Design	mixed-signal	mixed-signal	mixed-signal	mixed-signal
CMOS technology	180 nm	130 nm	130 nm	130 nm
Device type	**any BEOL current based**	RRAM	OxRAM	RRAM
Device terminals	**2-3**	2	2	2
Number of devices	19 k	65 k	4 k	3.14 M
Area including I/O	67.5 mm^2	-	-	158.76 mm^2
Core area	44.98 mm^2	1.79 mm^2	0.180 mm^2	-
Neuron model	AdExLIF	IF	IF	IF
Number of neurons	180	256	64	12 k
Number of synapses	10 k	65 k	4 k	3.14 M
Full parallel write	yes	-	column-wise	-
In-memory plasticity*	✓	✗	✗	✗
Learning rule	**STDP & SDSP**	-	S-STDP	-
Energy/spike NeuOp	25.9 pJ @ 80 Hz	0.0139 pJ/MAC	-	0.121 pJ

Chip	NElec'18 [35]	IEDM'19 [51]	VLSIT'19 [47]
Design	memristor	mixed-signal	mixed-signal
CMOS technology	-	130 nm	150 nm
Device type	HfO$_x$ RRAM	OxRAM	HfO$_x$ RRAM
Device terminals	2	2	2
Number of devices	74	13.5 k	64 k
Area including I/O	0.56 mm^2	-	-
Core area	-	-	-
Neuron model	stochastic LIF	IF	IF
Number of neurons	8	10	256
Number of synapses	64	1440	65 k
Full parallel write	yes	-	-
In-memory plasticity	✓	✗	✗
Learning rule	Hebbian LTP	-	-
Energy per spike/NeuOp	-	-	0.257 pJ/MAC

* The plasticity rule is implemented in-memory with local circuits, instead of off-crossbar generation of learning signals, eliminating off-array communication.

Table 2: **Comparison of TEXEL with other silicon-verified memristor-SNN chips.**
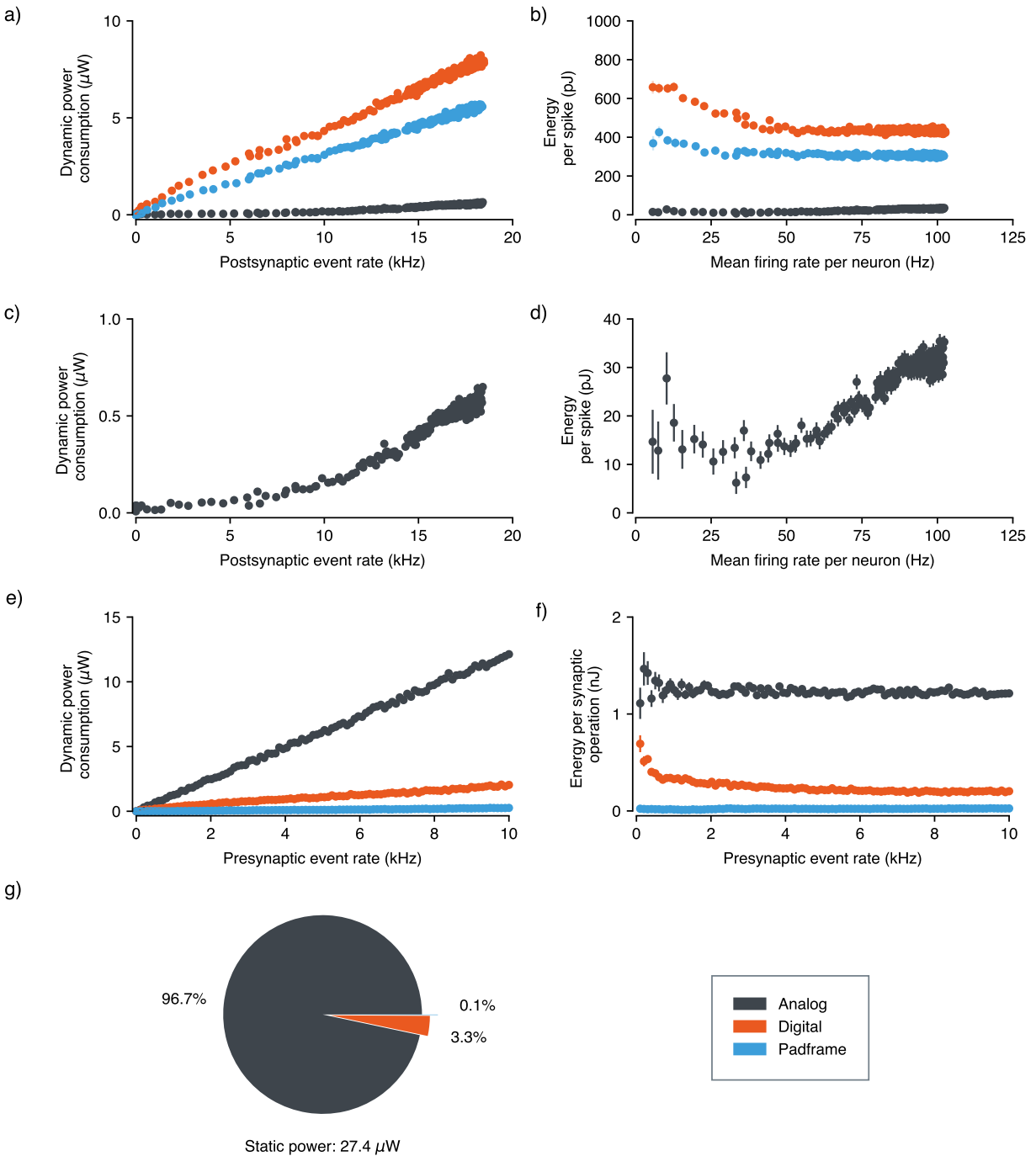
Fig. 5: **Dynamic and static power measurements of the TEXEL chip, focusing on energy consumption for synaptic operations and neuron spikes. a)** Dynamic power consumption versus postsynaptic event rate, measured for the three isolated power supplies. **b)** Energy per spike for increasing mean firing rates across each power supply. **c)** Dynamic power consumption of the analog power supply against postsynaptic event rate. **d)** Energy consumed per spike versus mean firing rate per neuron, for the analog power supply. **e)** Dynamic power consumption during random synaptic stimulation at increasing input event rates. **f)** Energy consumption per synaptic operation against input event rate. **g)** Breakdown of static power consumption while neurons are inactive and synapses are unstimulated.

or register block. The decoder translates external AER spike packets, while the encoder processes on-chip neuron spikes for transmission off-chip. The register block comprises 64 23-bit asynchronous memory arrays (per core) used for biasing and programming, each capable of parallel read or write operations. All analog circuitry is biased using a 12-bit Digital to Analog Converter (DAC) (see Supplementary Section A.3). To enable the integration of two- and three-terminal NVM devices there is interfacing circuitry including terminal contacts placed within each plastic synapse in every neuron block [1, 60, 61] (see Supplementary Fig. S3). Figure 1 shows the embedding of the neuron blocks and synapses within the chip architecture.

4.2 Neuron Circuits

The Adaptive Exponential Leaky Integrate-and-Fire (AdExLIF) neuron circuit integrated on TEXEL is the latest iteration of a continuing design evolution that has undergone multiple enhancements to optimize performance [1, 6, 19, 62–64]. The implementation of the neuron draws inspiration from the improvements detailed in [20], focusing on minimizing power consumption and reducing mismatch. The neuron dynamics are driven by two inputs: a DC input and a somatic input current from the synaptic fan-in, enabling network-level experiments. Figure 6a details the AdExLIF circuit, showing its distinct functional blocks. A somatic input DPI models the neuron's leak conductance, integrating synaptic currents into the membrane capacitance, producing a membrane current representing the neuron state variable [65]. Between the somatic DPI and spike generation, three modules control membrane current dynamics: a threshold, exponential and refractory module. The threshold module, implemented with a low-power current comparator, triggers a spike at the moment the membrane current exceeds the spiking threshold. The exponential module, implemented with a current-based positive feedback, accelerates the membrane current increase when it is closer to the spiking threshold. Once the neuron generates a spike, the refractory module keeps the neuron silent for a certain time set by the refractory period bias. Furthermore, there is an adaptation module, implemented with a pulse extender and a negative feedback low-pass filter circuit (DPI). This is activated with each output spike event, integrating the neuron's recent spiking activity. All aforementioned modules can be controlled using seven tunable biases. The neuron circuit is designed to be compatible with AER circuits therefore an asynchronous digital handshaking block is incorporated to transmit spikes as address-events through the AER pipeline.

4.3 Synaptic Circuits

Each neuron on the TEXEL chip has a synaptic fan-in of 58 synapses, 54 plastic and 4 non-plastic (static). Non-plastic synapses are realised through DPI circuits and activate in response to a presynaptic spike, producing a current with an amplitude that is tunable. Consequently, they can

be deactivated by setting the weight bias current to zero. The nature of the non-plastic synapses is predetermined, with two per-neuron designated as excitatory and two as inhibitory (Fig. 1b). The weight of the plastic synapses, updated according to the on-chip local learning rule, is stored on a capacitor on a short-time scale and discretized into two stable states on a long-time scale. The weight update occurs in the analog domain, while the long-term storage takes place in the digital domain. The nature of the plastic synapses (excitatory or inhibitory) can be configured on-chip. Excitatory synapses inject a positive current into the soma, while inhibitory ones draw current away from it. The total synaptic activity, computed as the sum of weighted currents, is transmitted to four different DPIs, each independently tunable.

4.4 Learning Circuits

Within each plastic synapse there exists a CMOS implementation of the BCaLL rule [66] that can be enabled, making use of signals local to each synapse to facilitate either Hebbian or anti-Hebbian Spike-Driven Synaptic Plasticity (SDSP) (Fig. 6b). A pre-trace, realised by a DPI circuit [46], maintains a decaying memory of the presynaptic spike train. If this trace exists between an upper and lower threshold then with the cooccurance of postsynaptic spikes the synaptic weight is depressed. In parallel, depression can also occur if the post-trace, a short term memory of postsynaptic activity, is above a low threshold and a presynaptic spike occurs. Potentiation occurs on a postsynaptic spike during which the value of the presynaptic trace is sampled from such that the magnitude of potentiation is proportional to the presynaptic trace at that time [25]. A smooth third trace, realised by a Second-order Differential Pair Integrator (SoDPI) circuit [67], is used to track the neurons' activity, representing the postsynaptic neuron's Ca^{2+} concentration. The upper and lower thresholds of the Ca^{2+} trace establish a "stop-learning" region, restricting synaptic plasticity to occur only within this range. The weight is stored as a voltage as shown in Figure 3a and is discretized via a voltage threshold. Additionally, a bistability circuit is employed such that over the long time scale the weight drifts towards a binary value. The temporal dynamics of the aforementioned traces, strength of the potentiation/depression events, bistability slew rates and thresholds can all be varied through the biasing of the analog circuitry.

4.5 Memristive Device Integration

To support large-scale integration of plastic memristor-based synapses, the chip is designed with a "device-agnostic" architecture, ensuring high flexibility and offering multiple probing configurations for different memristive devices. This design accommodates both two- and three-terminal devices, supporting a broad range of operating voltages and currents (see Table 1). Device behavior can be monitored either through on-chip read-outs of output currents during operation or via off-chip access to all
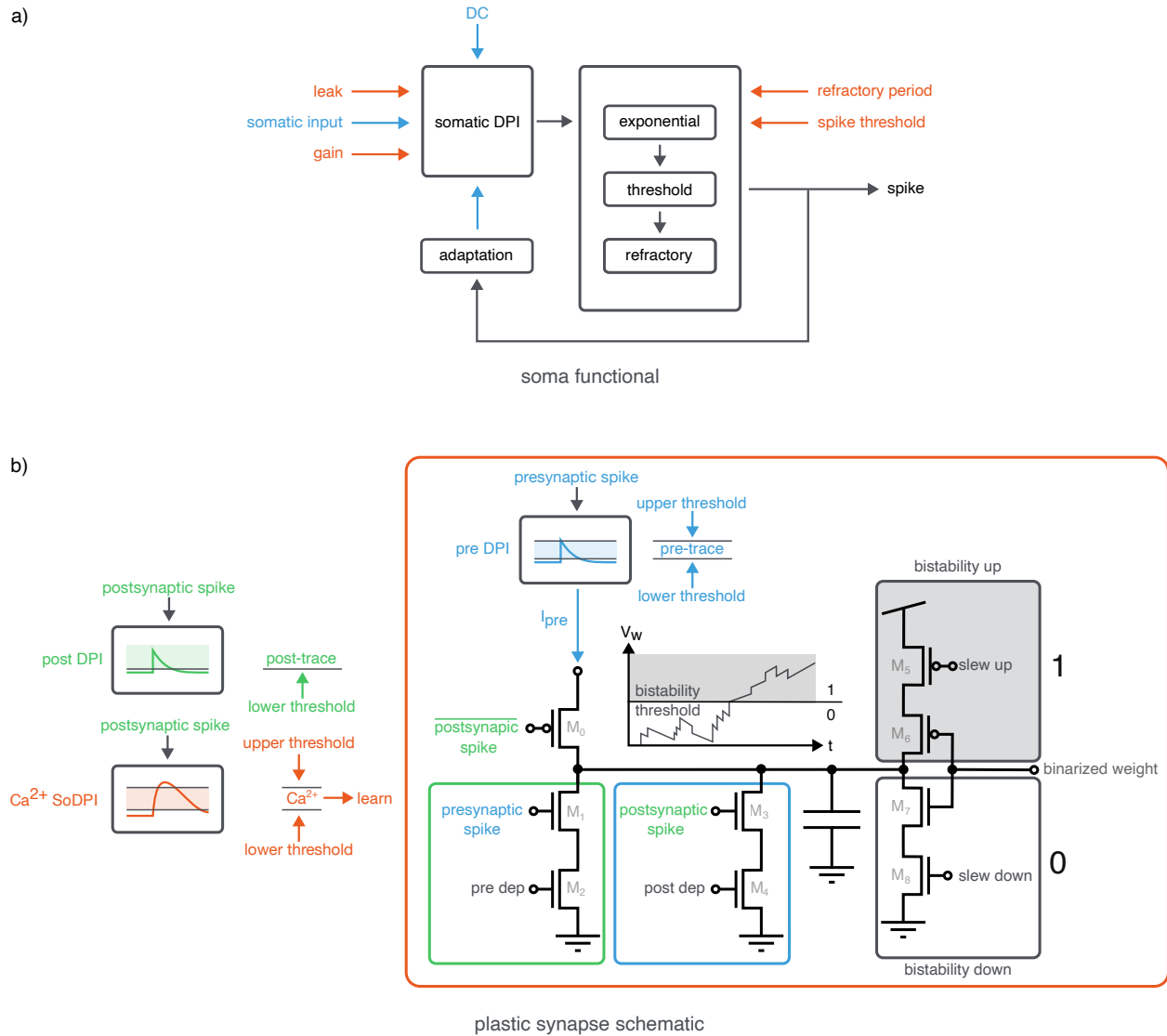
Fig. 6: **The functional architecture of the neuron on the TEXEL chip and schematic of the plasticity circuit in each plastic synapse. a)** The neuron features a somatic DPI that integrates input from both DC and synaptic sources, with circuits for thresholding, spike generation, refractory period, and positive feedback to mimic biological spiking neurons. An adaptation mechanism can be enabled to modulate spike frequency. Orange inputs represent tunable biases, and blue elements indicate current sources. **b)** The plasticity circuit in each synapse uses three analog traces to govern weight updates. Two neuron-level traces, the postsynaptic trace (post-trace) and the Ca^{2+} trace, are transmitted to synapses and must meet threshold conditions for weight updates. If the post-trace exceeds a threshold, incoming presynaptic spikes reduce the synaptic weight by a fixed increment. The presynaptic activity (pre-trace) also determines whether the weight will increase or decrease, with updates occurring via charge deposition on a capacitor. The weight is then quantized into high or low states by a bistability circuit, which controls drift toward ground or supply voltage, with drift rates set by the slew up and slew down biases.
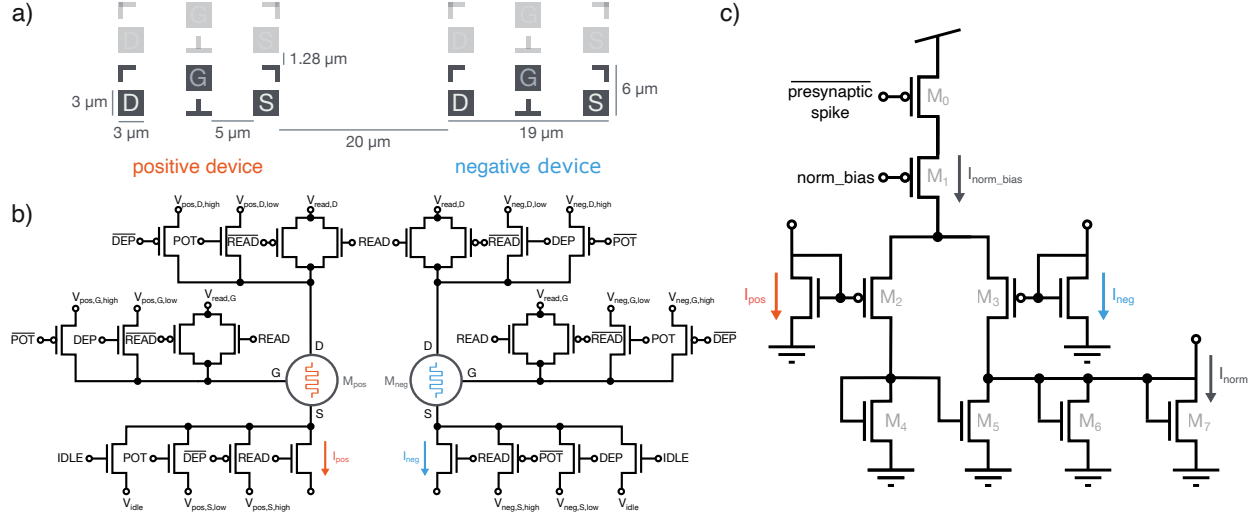
Fig. 7: **The footprint and schematic of the per-synapse device interface terminals and schematic of the differential normalizer circuit. a)** A diagram illustrating the physical dimensions and spatial arrangement of the source, drain, and gate contacts for two- or three-terminal devices. Each synapse deploys two devices configured differentially, serving as both positive and negative components. The diagram also provides information on the spacing between synaptic rows, depicting the distances between adjacent devices in each synapse. **b)** Schematic of device interface circuitry. All voltages can be set in the range 0–5 V in order to read or write both devices in the differential configuration. **c)** The differential normalizer circuit functions to compare the currents generated by positive and negative devices during a device read, prompted by a presynaptic spike. It evaluates the disparity between these currents and generates an output current, denoted as I_{norm}, which is proportional to the normalized discrepancy between I_{pos} and I_{neg}. Moreover, I_{norm} is exclusively non-zero when I_{pos} surpasses I_{neg} and can be modulated by the bias norm_bias. Consequently, the output represents the binary state of the synapse, and the sourced current is directed towards a DPI circuit for further processing.

device terminals through the interface circuit (see Supplementary Table 1). Full access to the device terminals enables external burn-in or programming of the memristive devices.

To facilitate BEOL integration, each terminal is accessible through a high-level metal contact with spacing and sizing depicted in Figure 7a. Three branches in the interface circuitry employ n- and p-type transistors, along with transmission gates, to deliver voltage pulses for reading device states or for potentiating or depressing synaptic weights (Fig. 7b). The operation voltages are provided off-chip as inputs to the padframe with a maximum voltage of 5 V. Digital signals to the transistor gates are internally controlled by a synapse controller circuit which implements synaptic operations and weight updates. We note that an extra idle transistor and idle signal is used to facilitate the possibility of pre-charging the device between read pulses and allow a better distinction between their High Resistance State (HRS) and Low Resistance State (LRS) currents (see Supplementary Section A.4).

Often, device operation specifications are not immediately compatible with the technology node and cannot be compensated for by voltage scaling or pulse length modulation. This can occur when currents are too low or too high, device variability is significant, or the resulting output ranges are undefined. In these cases, scaling and normalising circuits can be employed. Given this initial assumption

about the properties of a device aiming for compatibility, the TEXEL chip uses the difference in state of two devices to store the synaptic weight of each plastic synapse. Therefore the canonical on-chip operation protocol for memristive devices is binary and complementary. As a result, while using the on-chip plasticity, devices are only switched in a binary operation between HRS and LRS, and always in a complementary fashion where if one is in its HRS, the other will be in its LRS. A differential normalizer circuit is used to compare the responses of two devices [33] when the synaptic weight it being read. When the synapse is addressed for a read, at a presynaptic spike, the currents are sourced from the devices, I_{pos} and I_{neg}, and the normalizer circuit (Fig. 7c) rescales and rectifies the detected difference to the output current range required by the DPI synapse, I_{norm}. The rescaling factor of the output current can be modulated by the bias norm_bias.

Since many memristive devices use the same terminals for both reading and writing, they require exclusive control to prevent conflicts. In other words, when a read and write instruction occur simultaneously, a decision must be made regarding which operation to execute first. To manage this, each plastic synapse has a dedicated control circuit that ensures mutual exclusivity between read and write pulses (see Supplementary Fig. S2). Read instructions are prioritized, therefore if both commands occur concurrently, the write pulse is applied only after the read operation is completed.

5 Author Contributions

The following authors contributed significantly to the CMOS design of the TEXEL chip - A. R., E. C., G. I., H. G., J. C., M. C., M. F., M. M., O. R., P. K., W. S. G.

Conceptualisation - A. R., E. C., G. I., H. G., J. C., M. C., M. F., M. M., O. R., P. K., W. S. G.; Methodology - A. R. , E. C., G. I., H. G., J. C., M. C., M. F., M. M., O. R., P. K., W. S. G.; Software/Hardware - A. R., E. C., G. I., H. G., J. C., M. C., M. F., M. M., O. R., P. K., W. S. G.; Investigation - A. R. , E. C., G. I., H. G., M. M., O. R.; Writing - A. R., E. C., G. I., H. G., M. C., M. F., L. B. L., M. M., M. Z., O. R., P. K.; Visualisation - H. G., O. R., M. M., M.C., E. C., G. I.; Supervision - E. C., G. I.

6 Acknowledgements

7 Competing interests

The authors declare no competing interests.

References

[1] O. Richter *et al.*, "DYNAP-SE2: A scalable multi-core dynamic neuromorphic asynchronous spiking neural network processor", *Neuromorphic Computing and Engineering*, vol. 4, 2024. DOI: 10.1088/2634-4386/ad1cd7.

[2] C. Pehle *et al.*, "The BrainScales-2 accelerated neuromorphic system with hybrid plasticity", *Frontiers in Neuroscience*, vol. 16, p. 795 876, 2022. DOI: 10.3389/fnins.2022.795876.

[3] H. A. Gonzalez *et al.*, "Spinnaker2: A large-scale neuromorphic system for event-based and asynchronous machine learning", 2024. DOI: 10.48550/arXiv.2401.04491. arXiv: 2401.04491.

[4] G. Orchard *et al.*, "Efficient neuromorphic signal processing with Loihi 2", in *2021 IEEE Workshop on Signal Processing Systems (SiPS)*, 2021, pp. 254–259. DOI: 10.1109/SiPS52927.2021.00053.

[5] M. Davies *et al.*, "Loihi: A neuromorphic many-core processor with on-chip learning", *IEEE Micro*, vol. 38, no. 1, pp. 82–99, 2018. DOI: 10.1109/MM.2018.112130359.

[6] S. Moradi, N. Qiao, F. Stefanini, and G. Indiveri, "A scalable multicore architecture with heterogeneous memory structures for dynamic neuromorphic asynchronous processors (DYNAPs)", *IEEE Transactions on Biomedical Circuits and Systems*, vol. 12, no. 1, pp. 106–122, 2018. DOI: 10.1109/TBCAS.2017.2759700.

[7] B. V. Benjamin *et al.*, "Neurogrid: A mixed-analog-digital multichip system for large-scale neural simulations", *Proceedings of the IEEE*, vol. 102, no. 5, pp. 699–716, 2014. DOI: 10.1109/JPROC.2014.2313565.

[8] A. Sebastian, M. Le Gallo, R. Khaddam-Aljameh, and E. Eleftheriou, "Memory devices and applications for in-memory computing", *Nature nanotechnology*, vol. 15, no. 7, pp. 529–544, 2020. DOI: 10.1038/s41565-020-0655-z.

[9] D. V. Christensen *et al.*, "2022 Roadmap on neuromorphic computing and engineering", *Neuromorphic Computing and Engineering*, vol. 2, no. 2, p. 022 501, 2022. DOI: 10.1088/2634-4386/ac4a83.

[10] J. J. Yang, D. B. Strukov, and D. R. Stewart, "Memristive devices for computing", *Nature nanotechnology*, vol. 8, no. 1, pp. 13–24, 2013. DOI: 10.1038/nnano.2012.240.

[11] E. Chicca and G. Indiveri, "A recipe for creating ideal hybrid memristive-CMOS neuromorphic processing systems", *Applied Physics Letters*, vol. 116, no. 12, p. 120 501, 2020. DOI: 10.1063/1.5142089.

[12] H. Jia *et al.*, "15.1 a programmable neural-network inference accelerator based on scalable in-memory computing", in *2021 IEEE International Solid-State Circuits Conference (ISSCC)*, vol. 64, 2021, pp. 236–238. DOI: 10.1109/ISSCC42613.2021.9365788.

[13] B. Keller *et al.*, "A 17–95.6 TOPS/W deep learning inference accelerator with per-vector scaled 4-bit quantization for transformers in 5nm", in *2022 IEEE Symposium on VLSI Technology and Circuits (VLSI Technology and Circuits)*, 2022, pp. 16–17. DOI: 10.1109/VLSITechnologyandCir46769.2022.9830277.

[14] R. Khaddam-Aljameh *et al.*, "HERMES-core—a 1.59-TOPS/mm 2 PCM on 14-nm CMOS in-memory compute core using 300-ps/LSB linearized CCO-based ADCs", *IEEE Journal of Solid-State Circuits*, vol. 57, no. 4, pp. 1027–1038, 2022. DOI: `10.1109/JSSC.2022.3140414`.

[15] E. Donati, M. Payvand, N. Risi, R. Krause, and G. Indiveri, "Discrimination of emg signals using a neuromorphic implementation of a spiking neural network", *IEEE Transactions on Biomedical Circuits and Systems*, vol. 13, no. 5, pp. 795–803, 2019. DOI: `10.1109/TBCAS.2019.2925454`.

[16] V. Fra, E. Forno, R. Pignari, T. C. Stewart, E. Macii, and G. Urgese, "Human activity recognition: Suitability of a neuromorphic approach for on-edge aiot applications", *Neuromorphic Computing and Engineering*, vol. 2, no. 1, p. 014 006, 2022. DOI: `10.1088/2634-4386/ac4c38`.

[17] O. Gallou, J. Bartels, S. Ghosh, K. Schindler, J. Sarnthein, and G. Indiveri, "Online epileptic seizure detection in long-term ieeg recordings using mixed-signal neuromorphic circuits", *medRxiv*, 2024. DOI: `10.1101/2024.06.13.24308876`.

[18] S. C. Liu, J. Kramer, G. Indiveri, T. Delbruck, and R. J. Douglas, *Analog VLSI: circuits and principles*. 2002. DOI: `10.7551/mitpress/1250.001.0001`.

[19] E. Chicca, F. Stefanini, C. Bartolozzi, and G. Indiveri, "Neuromorphic electronic circuits for building autonomous cognitive systems", *Proceedings of the IEEE*, vol. 102, no. 9, pp. 1367–1388, 2014. DOI: `10.1109/JPROC.2014.2313954`.

[20] A. Rubino, C. Livanelioglu, N. Qiao, M. Payvand, and G. Indiveri, "Ultra-low-power FDSOI neural circuits for extreme-edge neuromorphic intelligence", *IEEE Transactions on Circuits and Systems I: Regular Papers*, vol. 68, no. 1, pp. 45–56, 2021. DOI: `10.1109/TCSI.2020.3035575`.

[21] L. Khacef, P. Klein, M. Cartiglia, A. Rubino, G. Indiveri, and E. Chicca, "Spike-based local synaptic plasticity: A survey of computational models and neuromorphic circuits", *Neuromorphic Computing and Engineering*, vol. 3, no. 4, p. 042 001, 2023. DOI: `10.1088/2634-4386/ad05da`.

[22] R. George *et al.*, "Plasticity and adaptation in neuromorphic biohybrid systems", *Iscience*, vol. 23, no. 10, 2020. DOI: `10.1016/j.isci.2020.101589`.

[23] N. Qiao *et al.*, "A re-configurable on-line learning spiking neuromorphic processor comprising 256 neurons and 128K synapses", *Frontiers in Neuroscience*, vol. 9, no. 141, 2015. DOI: `10.3389/fnins.2015.00141`.

[24] E. Chicca *et al.*, "A VLSI recurrent network of integrate–and–fire neurons connected by plastic synapses with long–term memory", *IEEE Transactions on Neural Networks*, vol. 14, no. 5, pp. 1297–1307, 2003. DOI: `10.1109/TNN.2003.816367`.

[25] G. Indiveri, E. Chicca, and R. J. Douglas, "A VLSI array of low-power spiking neurons and bistable synapses with spike–timing dependent plasticity", *IEEE Transactions on Neural Networks*, vol. 17, no. 1, pp. 211–221, 2006. DOI: `10.1109/TNN.2005.860850`.

[26] J. Bartol Thomas M *et al.*, "Nanoconnectomic upper bound on the variability of synaptic plasticity", *eLife*, vol. 4, e10778, 2015. DOI: `10.7554/eLife.10778`.

[27] D. J. Amit and S. Fusi, "Learning in neural networks with material synapses", *Neural Computation*, vol. 6, no. 5, pp. 957–982, 1994. DOI: `10.1162/neco.1994.6.5.957`.

[28] M. Cartiglia *et al.*, "Stochastic dendrites enable online learning in mixed-signal neuromorphic processing systems", in *2022 IEEE International Symposium on Circuits and Systems (ISCAS)*, 2022, pp. 476–480. DOI: `10.1109/ISCAS48785.2022.9937833`.

[29] S. D'Agostino *et al.*, "DenRAM: Neuromorphic dendritic architecture with RRAM for efficient temporal processing with delays", *Nature communications*, vol. 15, no. 1, p. 3446, 2024. DOI: `10.1038/s41467-024-47764-w`.

[30] X. Zhang *et al.*, "Hybrid memristor-CMOS neurons for in-situ learning in fully hardware memristive spiking neural networks", *Science Bulletin*, vol. 66, no. 16, pp. 1624–1633, 2021. DOI: `10.1016/j.scib.2021.04.014`.

[31] M. Payvand, M. E. Fouda, F. Kurdahi, A. M. Eltawil, and E. O. Neftci, "On-chip error-triggered learning of multi-layer memristive spiking neural networks", *IEEE Journal on Emerging and Selected Topics in Circuits and Systems*, vol. 10, no. 4, pp. 522–535, 2020. DOI: `10.1109/JETCAS.2020.3040248`.

[32] L. A. Camuñas-Mesa, E. Vianello, C. Reita, T. Serrano-Gotarredona, and B. Linares-Barranco, "A CMOL-like memristor-CMOS neuromorphic chipcore demonstrating stochastic binary STDP", *IEEE Journal on Emerging and Selected Topics in Circuits and Systems*, vol. 12, no. 4, pp. 898–912, 2022. DOI: `10.1109/JETCAS.2022.3207514`.

[33] M. V. Nair, L. K. Muller, and G. Indiveri, "A differential memristive synapse circuit for on-line learning in neuromorphic computing systems", *Nano Futures*, vol. 1, no. 3, p. 035 003, 2017.

[34] Z. Zhao *et al.*, "A memristor-based spiking neural network with high scalability and learning efficiency", *IEEE Transactions on Circuits and Systems II: Express Briefs*, vol. 67, no. 5, pp. 931–935, 2020. DOI: `10.1109/TCSII.2020.2980054`.

[35] Z. Wang *et al.*, "Fully memristive neural networks for pattern classification with unsupervised learning", *Nature Electronics*, vol. 1, no. 2, pp. 137–145, 2018. DOI: `10.1038/s41928-018-0023-2`.

[36] S. Song, K. Miller, and L. Abbot, "Competitive Hebbian learning through spike-timing-dependent plasticity", *Nature Neuroscience*, vol. 3, no. 9, pp. 919–926, 2000. DOI: 10.1038/78829.

[37] J. Brader, W. Senn, and S. Fusi, "Learning real world stimuli in a neural network with spike-driven synaptic dynamics", *Neural Computation*, vol. 19, pp. 2881–2912, 2007. DOI: 10.1162/neco.2007.19.11.2881.

[38] N. Perez-Nieves, V. C. Leung, P. L. Dragotti, and D. F. Goodman, "Neural heterogeneity promotes robust learning", *Nature communications*, vol. 12, no. 1, p. 5791, 2021. DOI: 10.1038/s41467-021-26022-3.

[39] W. Soares Girão, N. Risi, and E. Chicca, "Learning in spiking neural networks with a calcium-based hebbian rule for spike time-dependent plasticity", *in preparation*, 2024.

[40] D. O. Hebb, *The organization of behavior: a neuropsychological theory*. 1949. DOI: 10.4324/9781410612403.

[41] W. Senn and S. Fusi, "Learning only when necessary: Better memories of correlated patterns in networks with bounded synapses", *Neural Computation*, vol. 17, no. 10, pp. 2106–2138, 2005. DOI: 10.1162/0899766054615644.

[42] S. Mitra, S. Fusi, and G. Indiveri, "Real-time classification of complex patterns using spike-based learning in neuromorphic VLSI", *IEEE Transactions on Biomedical Circuits and Systems*, vol. 3, no. 1, pp. 32–42, 2009. DOI: 10.1109/TBCAS.2008.2005781.

[43] A. Rubino, M. Cartiglia, M. Payvand, and G. Indiveri, "Neuromorphic analog circuits for robust on-chip always-on learning in spiking neural networks", in *2023 IEEE 5th International Conference on Artificial Intelligence Circuits and Systems (AICAS)*, 2023, pp. 1–5. DOI: 10.1109/AICAS57966.2023.10168620.

[44] M. Bocquet *et al.*, "In-memory and error-immune differential RRAM implementation of binarized deep neural networks", in *2018 IEEE International Electron Devices Meeting (IEDM)*, 2018, pp. 20.6.1–20.6.4. DOI: 10.1109/IEDM.2018.8614639.

[45] T. Hirtzlin *et al.*, "Digital biologically plausible implementation of binarized neural networks with differential hafnium oxide resistive memory arrays", *Frontiers in Neuroscience*, vol. 13, 2020. DOI: 10.3389/fnins.2019.01383.

[46] C. Bartolozzi and G. Indiveri, "Synaptic dynamics in analog VLSI", *Neural Computation*, vol. 19, no. 10, pp. 2581–2603, 2007. DOI: 10.1162/neco.2007.19.10.2581.

[47] B. Yan *et al.*, "RRAM-based Spiking Nonvolatile Computing-In-Memory Processing Engine with Precision-Configurable In Situ Nonlinear Activation", in *2019 Symposium on VLSI Technology*,

2019, T86–T87. DOI: 10.23919/VLSIT.2019.8776485.

[48] W. Wan *et al.*, "33.1 A 74 TMACS/W CMOS-RRAM Neurosynaptic Core with Dynamically Reconfigurable Dataflow and In-situ Transposable Weights for Probabilistic Graphical Models", in *2020 IEEE International Solid- State Circuits Conference - (ISSCC)*, 2020, pp. 498–500. DOI: 10.1109/ISSCC19947.2020.9062979.

[49] W. Wan *et al.*, "A compute-in-memory chip based on resistive random-access memory", *Nature*, vol. 608, no. 7923, pp. 504–512, 2022. DOI: 10.1038/s41586-022-04992-8.

[50] I. D. De Los Ríos, L. Camuñas-Mesa, E. Vianello, C. Reita, T. Serrano-Gotarredona, and B. Linares-Barranco, "A multi-core memristor chip for Stochastic Binary STDP", in *2023 IEEE International Symposium on Circuits and Systems (ISCAS)*, 2023, pp. 1–5. DOI: 10.1109/ISCAS46773.2023.10181899.

[51] A. Valentian *et al.*, "Fully integrated spiking neural network with analog neurons and RRAM synapses", in *2019 IEEE International Electron Devices Meeting (IEDM)*, IEEE, 2019, pp. 14–3. DOI: 10.1109/IEDM19573.2019.8993431.

[52] D. F. Falcone, M. Halter, L. Bégon-Lours, and B. J. Offrein, "Back-end, CMOS-compatible ferroelectric FinFET for synaptic weights", *Frontiers in Electronic Materials*, vol. 2, p. 849879, 2022. DOI: 10.3389/femat.2022.849879.

[53] S. Dutta *et al.*, "Logic compatible high-performance ferroelectric transistor memory", *IEEE Electron Device Letters*, vol. 43, no. 3, pp. 382–385, 2022. DOI: 10.1109/LED.2022.3148669.

[54] S. Choi, J. Yang, and G. Wang, "Emerging memristive artificial synapses and neurons for energy-efficient neuromorphic computing", *Advanced Materials*, vol. 32, no. 51, p. 2004659, 2020. DOI: 10.1002/adma.202004659.

[55] Y. Demirağ *et al.*, "PCM-trace: Scalable synaptic eligibility traces with resistivity drift of phase-change materials", in *2021 IEEE International Symposium on Circuits and Systems (ISCAS)*, 2021, pp. 1–5. DOI: 10.1109/ISCAS51556.2021.9401446.

[56] S. Dai *et al.*, "Emerging iontronic neural devices for neuromorphic sensory computing", *Advanced Materials*, vol. 35, no. 39, p. 2300329, 2023. DOI: 10.1002/adma.202300329.

[57] C. Lenk *et al.*, "Neuromorphic acoustic sensing using an adaptive microelectromechanical cochlea with integrated feedback", *Nature Electronics*, vol. 6, no. 5, pp. 370–380, 2023. DOI: 10.1038/s41928-023-00957-5.

[58] T. Dalgaty *et al.*, "Mosaic: In-memory computing and routing for small-world spike-based neuromorphic systems", *Nature Communications*, vol. 15,

no. 1, p. 142, 2024. DOI: 10.1038/s41467-023-44365-x.

[59] S. Ataei *et al.*, "An open-source eda flow for asynchronous logic", *IEEE Design & Test*, vol. 38, no. 2, pp. 27–37, 2021. DOI: 10.1109/MDAT.2021.3051334.

[60] A. Neckar *et al.*, "Braindrop: A mixed-signal neuromorphic architecture with a dynamical systems-based programming model", *Proceedings of the IEEE*, vol. 107, no. 1, pp. 144–164, 2019. DOI: 10.1109/JPROC.2018.2881432.

[61] J. Park, S. Ha, T. Yu, E. Neftci, and G. Cauwenberghs, "A 22-pJ/spike 73-Mspikes/s 130k-compartment neural array transceiver with conductance-based synaptic and membrane dynamics", *Frontiers in Neuroscience*, vol. 17, p. 1 198 306, 2023. DOI: 10.3389/fnins.2023.1198306.

[62] G. Indiveri, "Neuromorphic selective attention systems", in *International symposium on circuits and systems, ISCAS 2003*, 2003, pp. III–770–III–773. DOI: 10.1109/ISCAS.2003.1205133.

[63] P. Livi and G. Indiveri, "A current-mode conductance-based silicon neuron for address-event neuromorphic systems", in *2009 IEEE International Symposium on Circuits and Systems*, IEEE, 2009, pp. 2898–2901. DOI: 10.1109/ISCAS.2009.5118408.

[64] N. Qiao, C. Bartolozzi, and G. Indiveri, "Automatic gain control of ultra-low leakage synaptic scaling homeostatic plasticity circuits", in *Biomedical circuits and systems conference, (BioCAS), 2016*, 2016, pp. 156–159. DOI: 10.1109/BioCAS.2016.7833755.

[65] C. Bartolozzi, "Selective attention in silicon: From the design of an analog VLSI synapse to the implementation of a multi–chip system," PhD thesis, 2007. DOI: 10.3929/ethz-a-005462057.

[66] W. Soares Girão *et al.*, "A subthreshold CMOS hardware implementation of a bistable calcium-based local learning rule", *in preparation*, 2024.

[67] O. Richter *et al.*, "A subthreshold second-order integration circuit for versatile synaptic alpha kernel and trace generation", in *Proceedings of the 2023 International Conference on Neuromorphic Systems*, 2023, pp. 1–4. DOI: 10.1145/3589737.3606008.

A Supplementary Materials

A.1 Signal Monitoring

TEXEL provides several methods to observe the internal state of various components, circuits and signals. There are three distinct monitoring methods shown in Table 1 under the "Domain" column. The first are analog outputs, they provide access to real time signals measurable by an oscilloscope or Analog Digital Converters (ADCs). The second monitoring method are digital output pins which expose internal digital signals. The third is the asynchronous sADCs interface.

When using the sADC bank, the current under observation is mirrored inside a circuit (described in depth in [1]) that generates a spike rate proportional to the current magnitude. The spikes are propagated through an encoder interfaced with a dedicated 5 bit AER bus. The sADC bank allows the user to monitor 49682 currents, of which 24 simultaneously. Structures that convert currents into spikes for monitoring are popular solutions in literature with several known implementations [1–4]. In many cases, the signal under observation can be selected across synapses and neurons. This is denoted by the "Mux" column in Table 1.

Figure 3 offers an example of how the monitoring methods can be used. In the first row, for example, the presynaptic trace current (I_{PRE}) of a synapse is shown while it receives an input spike train. The synapse has been selected among all the available synapses but setting a register inside the chip through the input AER bus. I_{PRE} is recorded using the sADC and the spiking activity of the sADC is transmitted through the dedicated AER bus. The spikes recorded by the Microcontroller (μC) are used to reconstruct the dynamics of the signal. This is done by finding the Interspike Interval (ISI) of the spike train and taking the reciprocal to calculate the instantaneous spike rate at the corresponding spike time. The resulting current proxy is visible in Figure 3a, using the instantaneous firing rate. The same procedure is repeated for the I_{POST} and the $\text{Ca}^{2+}_{\text{below}}$ current traces, depicted in the same Figure 3a. It is noted that the sADC spiking output is able to capture dynamics on three different time scales effectively ($10\,\text{ms}$ for I_{PRE}, $100\,\text{ms}$ for I_{POST} and $1\,\text{s}$ for the $\text{Ca}^{2+}_{\text{below}}$ trace). In the second row of Figure 3a, we see another example of the monitoring capability of the chip: V_{mem}, the membrane voltage of the neuron. Using the same procedure explained for the synapse, a specific neuron is chosen for monitoring. This outputs the membrane potential of the neuron on a Bayonet-Neill-Concelman (BNC) cable. For synaptic signals, V_{w} can be observed in the last row of Figure 3a, by selecting it through a monitoring register.

A.2 sADC

On the TEXEL chip 49682 currents can be monitored, of which 24 simultaneously. This is possible thanks to the implementation of the sADC [1]. The circuit follows a mixed signal approach, where the analog block continuously interacts with the asynchronous digital block in a way inspired by mixed-signal implementations of spiking neurons. The working principle of the sADC is as follows: the current under monitoring is mirrored from the circuit and fed in the input of the sADC. This current is directed towards the negative input node of a Operational Amplifier (OPAMP), connected through a capacitor C_{mem}, to the OPAMP's output, generating a negative feedback loop. The negative feedback loop, under ideal conditions, allows for the creation of a virtual ground: the negative input node of the OPAMP stabilizes its voltage close to ref_h, regardless of the input current received, while allowing the input current to charge C_{mem}. Charging the capacitor with said current, while the transistor gate (M_1) stays at a fixed voltage, results in an increasing output voltage, which is sensed by a the subsequent circuit. This circuit is composed of a hysteresis-equipped Operational Transconductance Amplifier (OTA) which implements a threshold function. Here, the input voltage is compared to a fixed bias, and only when the input is above a certain voltage $\text{CF}_{\text{REF}-\text{L}} + V_{\text{HYS}}$, the output changes its digital state. The switch of the output state activates the asynchronous digital interface (HS), generating a request for a spike event. Once the circuit receives the acknowledgement signal from the subsequent digital block, the reset of the integrated current begins: a digital pulse completely discharges capacitor C_{refr}, which is then promptly charged back by a constant current CF_{PWLK}. The time taken by this capacitor to be charged sets the refractory period of the circuit. During this time, in fact, the capacitor C_{mem} has its terminals shorted by an active transistor (M_1), inhibiting the ability to charge with input currents. When no acknowledgement is detected, a pull-up is actively keeping the capacitor C_{refr} charged. The behaviour of the sADC versus an input current can be seen in Figure S1b, where, using a programmable DAC, the input current has been swept logarithmically between $1\,\text{pA}$ to $1\,\text{nA}$. One can notice the very wide range of frequency at the output that demonstrates the ability of the circuit to monitor a very wide range of input currents.

The tuning parameters for the circuit are:

- EN: a digital flag determining whether the sADC should receive inputs from the monitored signals or from off_bias.
- off_bias, a fixed bias current alternative to the input current.

Name	Description	Type	Domain	Port	Mux
I_{DAC}	Current of a single DAC (for calibration)	Current	Frequency	sADC	-
I_{PRE}	Pre trace of the plastic synapse	Current	Frequency	sADC	SYN
I_{SO}	Second order trace of the Ca^{2+} SoDPI trace	Current	Frequency	sADC	NRN
I_{POST}	Post trace of the neuron	Current	Frequency	sADC	NRN
$I_{\text{P-LEFT}}$	Current of the plastic left synapse	Current	Frequency	sADC	SYN
$I_{\text{P-RIGHT}}$	Current of the plastic right synapse	Current	Frequency	sADC	SYN
$I_{\text{S-EXC}}$	Current of the static excitatory synapse	Current	Frequency	sADC	NRN
I_{AHP}	Adaptive current of the neuron	Current	Frequency	sADC	NRN
I_{FO}	First order trace of the Ca^{2+} SoDPI trace	Current	Frequency	sADC	NRN
$I_{\text{S-INH}}$	Current of the static inhibitory synapse	Current	Frequency	sADC	NRN
V_{MEM}	Membrane voltage of the neuron	Voltage	Analog	BNC	NRN
V_{W}	Analog weight of plastic synapse	Voltage	Analog	BNC	SYN
I_{DAC}	Current of a single DAC (for calibration)	Current	Analog	BNC	-
$\text{Ca}^{2+}_{\text{ABOVE}}$	Ca^{2+} above high threshold	Voltage	Digital	Pin	NRN
$\text{Ca}^{2+}_{\text{BELOW}}$	Ca^{2+} below low threshold	Voltage	Digital	Pin	NRN
$\text{POST}_{\text{ABOVE}}$	Post trace above high threshold	Voltage	Digital	Pin	NRN
W_{SYN}	Digitized V_{W}	Voltage	Digital	Pin	SYN
Device Monitoring					
$I_{\text{DEV-NEG}}$	Current from negative device	Current	Frequency	sADC	SYN
$I_{\text{DEV-NORM}}$	Current from normalizer circuit	Current	Frequency	sADC	SYN
DEV_{READ}	Device read pulse	Voltage	Digital	Pin	SYN
$\text{DEV}_{\text{WRITE}}$	Device write pulse	Voltage	Digital	Pin	SYN
DEV_{INT}	Device interrupt flag	Voltage	Digital	Pin	SYN
$\text{DEV}_{\text{STATE}}$	Device state	Voltage	Digital	Pin	SYN

Table 1: **Signals that can be monitored on the TEXEL chip.** The table is divided into three blocks: current signals observable through the spiking output of the sADCs; voltage and current outputs measurable through BNC connectors; and digital flags measurable on output pins.

- ref_h: The voltage at which the virtual ground should be set. This voltage shifts the low node of the capacitor C_{mem}.
- bias: the current at which the OPAMP should be biased: it defines the strength of the feedback loop (so the ability of the circuit to keep the virtual ground to a specific voltage regardless of the input current magnitude and speed).
- ref_l: The voltage at which the capacitor's positive node is compared in the OTA.
- hys: the current deciding the hysteresis value of the OTA. This defines how much capacitor positive node should be offset with respect to ref_l, to elicit a spike, such that $V_{\text{mem}} > \text{ref\_l} + V_{\text{hys}}$.
- pwlk: the leakage of the refractory transistor, this parameter sets how long should the circuit wait before being able to integrate current again.

A.3   DAC

Each core incorporates a fully programmable 94-channel 12-bit DAC, capable of generating reference currents and parameters ranging from $0.5\,\text{pA}$ to $2.2\,\mu\text{A}$, inspired by the design proposed in [5]. These parameters serve to configure the operation settings for the neuron, synapse and learning circuits, as well as control the timing of the device interface.

| (a) sADC schematic | (b) sADC response |
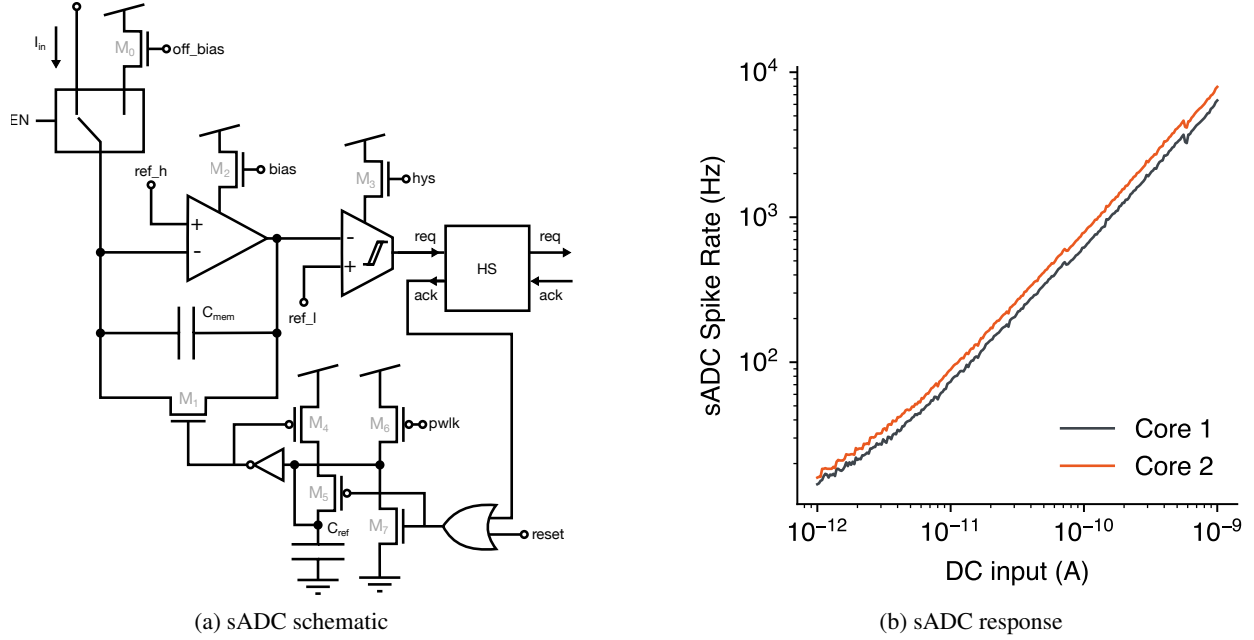
Fig. S1: **sADC circuit and the measurements of the spike rate in response to DC input. a)** sADC schematic with biases labelled. The input current is converted to a spikes and is transmitted via the handshake (HS) block and encoded as an address representing the signal being monitored by the sADC. **b)** Spiking response of two sADC circuits (one on each core) in response to a logarithmic sweep of DC input current from an on-chip DAC. The mapping between current and spike rate obeys a power law, these measurements show how the spike rate of an sADC can be used to infer the magnitude of its input current. The core-to-core deviation is due to mismatch.

The DAC is comprised of three components: first, the configuration storage, which is part of the digital blocks. Second, the reference current generator, responsible for producing six reference currents. Third, the 1T-2T current dividers to generate channel currents from these references. The reference current segment employs a subthreshold CMOS and resistor Proportional To Absolute Temperature (PTAT) source, augmented by a current divider block that incorporates a resistor in the divider to function as a Complementary To Absolute Temperature (CTAT) source. Together with the PTAT, this combination reduces the temperature sensitivity. The resulting current is directed into scaling current mirrors and conveyors to generate scaled base currents (master currents). In this instance, master currents include values of $2.2\,\mu A$, $0.29\,\mu A$, $36\,nA$, $4.5\,nA$, $0.57\,nA$, and $70\,pA$. For each channel, one of these currents is chosen. The resulting current is then passed to a finer division stage of 8 bits, providing 256 levels, with the last selection per channel determining whether the current is sourced by an nFET or a pFET. The fine division stage is composed of MOSFETs substituting resistors in the common 1R-2R DAC circuit (here called 1T-2T). Due to the fact that the current divider employs MOSFETs instead of resistors, the saturation condition of the transistors need to be guarded. The result of the violation of the saturation condition of the MOSFET is the DAC not being entirely monotonic.

A.4 Device Operation & Integration

A.4.1 Synapse Controller

We conducted chip measurements to verify the functionality of the synapse controller. The synapse controller constitutes circuitry at each synapse which manages cases where read and write operations overlap. Three scenarios of read-write interactions are examined through read and write protocols, with digital pins capturing read, write, and interrupt pulses, and weight changes monitored via analog channels. The controller appropriately prioritizes read operations over writes, as evidenced by the detection of interrupt flags when a read coincides with a write pulse, and then executes the write; this ensures correct device operation (Fig. S2).

A.4.2 Continuous Read

In addition to the aforementioned device operation mode, the TEXEL platform can be configured to a "continuous read" mode. In this mode the READ signal is permanently set to high such that the drain of the device is held at $V_{read,D}$, the gate is held at $V_{read,G}$ and the source is connected to both input branches of the normalizer circuit (Fig. 7). This READ

3

state is mutually exclusive with respect to memristive device writing signals (POT/DEP). In this mode the IDLE signal becomes obsolete and is held at ground. This "continuous read"" mode would be used in the case for which the memristive device capacitance is high and potentially outside "compatibility" range derived from simulations.

A.4.3 Transition-Metal Oxides

Two-terminal memristive devices consisting of one or more layers of transition metal oxides are widely used for neuromorphic systems, especially for emulating synaptic functions [6]. Here we evaluate three-layer memristive device stacks for their integration into the TEXEL platform. The layer sequence of the memristive device considered for this purpose is HfO_x /Al_2O_3 /TiO_2, embedded between an Au contact layer and the TiN bottom electrode [7]. Here, the HfO_x is responsible for the memristive behavior, the Al_2O_3 changes the interface properties and the TiO_2 layer is advantageous because it forms well-defined interfaces with the TiN electrode and the Al_2O_3 intermediate layer. Furthermore, the Al_2O_3 layer controls the generation of oxygen vacancies and thus serves to limit the current. This is particularly important for integrating the devices into circuits in order to operate the devices without a current compliance.

The stoichiometry of the HfO_x layer is decisive for the resistive switching mechanism [7]. Particularly for sub-stoichiometric oxides (x between 1.5 and 1.8), filamentary switching is observed, while stoichiometric oxide layers ($x = 2$) have an interface-based switching mechanism. However, this leads to different device properties. Gradual resistance switching is observed in interface switching devices, while devices based on filamentary switching exhibit a more abrupt switching characteristic. In the latter, however, multi-level resistance states can be achieved by careful design of the oxygen-vacancy filament. However, the two classes of devices have different requirements that need to be considered when integrating them into the TEXEL platform, which we have analyzed below. Both types of switching devices were fabricated in a thin-film technology using reactive DC magnetron sputtering. This was used to deposit the layers of the device stack with the following thicknesses: HfO_x has a thickness of $3\,nm$, Al_2O_3 of $2\,nm$ and TiO_2 of $15\,nm$. The device electrodes are electrically insulated by a $180\,nm$ thick SiO_2 layer, encapsulating the functional layers. A $30\,nm$ thick Au layer defines the top electrode and are used to define the active device area. Further details on the device fabrication can be found in [7].

Interface switching devices: The resistance values for this class of devices are between $0.7\,M\Omega$ and $290\,M\Omega$, depending on the concentration of oxygen vacancies in the active memristive HfOx layer. Here, R_{on}/R_{off} ratios of up to 10^{-3} are achieved. The switching voltages required for this are $2.5\,V$ or $3.5\,V$ for setting the devices and $-1.5\,V$ or $-3\,V$ for resetting. This corresponds to current values of $3.6\,\mu A$ and $10\,nA$ as well as $-2.1\,\mu A$ and $-10\,nA$. In other words, values that are compatible with the TEXEL platform (Fig. 4c). However, these values are dependent on the device area and were determined for an area of $20\,\mu m^2$. For a direct integration of these devices on the contact areas shown in Fig. 7a, a reduction of the device area by a factor of about 10 is necessary. However, this would be accompanied by a moderate increase in resistance. This can be estimated from a resistance value in the off state of $20\,M\Omega$ for the current area size to $40\,M\Omega$ - $50\,M\Omega$ if the device area size is reduced by a factor of 10. Values that the TEXEL platform allows.

Another important device parameter that must be determined and adapted for the integration of the devices into the TEXEL platform is the device/layer capacitance. The layer capacitance of the transition metal oxides in the layer thickness range used here can be estimated in the range of $10^{-14}\,F\,\mu m^{-2}$ [8], which fulfils the requirements of the TEXEL platform given in Fig. 4d.

Filamentary switching devices: For filamentary memristive devices, the resistance values of the off resistance are in the range of $0.16\,M\Omega$ - $80\,M\Omega$ depending on the concentration of oxygen vacancies in the HfO_x layer [7]. Voltages from -1.5–$-3.0\,V$ are required for setting the devices, while resetting requires voltages in the range 2.5–$3.0\,V$. This can be converted into current values in the range $-20\,\mu A$ to $-20\,nA$ for the setting process and $15\,\mu A$ to $40\,nA$ for the resetting process. The R_{on}/R_{off} ratio with is 10^{-1}–10^{-2}, slightly smaller compared to interface switching devices, but fulfils the requirements of the TEXEL platform very well, as shown in Fig. 4c. Capacitance is determined by the device area as well as the filament area. The relevant size for integration is the device area capacitance, which we assume to be $10^{-14}\,F\,\mu m^{-2}$ as in the case of interface switching devices. The scaling of the device area has no influence on the resistance values. However, an inertial forming step is required for these devices, which requires voltages of up to $\pm 5\,V$, which is compatible with the TEXEL platform.

A.4.4 Ferroelectric Hafnia

Two- and three-terminal synaptic weights based on ferroelectric hafnia are evaluated for their integration on the TEXEL platform. In the two-terminal configuration, the current flows through the ferroelectric layer, which requires the layer thickness to be scaled while maintaining a high polarization. The materials were specifically developed on the XFAB $180\,nm$ technology, replicating the conditions for integration on the TEXEL platform. The conductivity and the dynamic

range of the BEOL-integrated synaptic weights were found to differ from the same weights nanofabricated on dummy Si wafers [9]. The $2\,\mathrm{V}$ required to operate the synaptic weights fall well in the range available in TEXEL. The dynamic range falls between 1 and 10, for which the optimal resistance is predicted to be in the $10\,\mathrm{G\Omega}$ range. It would result in an average current sourced by the differential normalizer synapse of two thirds of norm_bias. The scalability of the resistance with the area allows to adapt the design to the current requirement: an ideal resistance of $10\,\mathrm{G\Omega}$ is obtained by scaling the device to $10\,\mathrm{\mu m^2}$.

In the three-terminal configuration (FeFET or thin-film transistor) the ferroelectric gate is integrated prior to the semiconducting oxide channel. The materials optimized for the fabrication of two-terminal devices on TEXEL were evaluated for three-terminal devices, i.e. with an increased gate thickness up to $10\,\mathrm{nm}$. In test circuits, the ferroelectric switching of the capacitors was demonstrated through the same interconnects and transistors that on the TEXEL platform [10]. The saturation for the ferroelectric switching is obtained for $\pm 4\,\mathrm{V}$, in line with the device requirements.

The CMOS-compatibility translates in the absence of degradation of the front-end electronics during the back-end integration of the synaptic weights. For the ferroelectric technology presented above, the critical steps are:

1. the deposition of a functional tungsten oxide layer at $375\,^\circ\mathrm{C}$ under an oxidizing plasma
2. the crystallization of hafnia in the ferroelectric phase

It uses a flash lamp annealer applying a $20\,\mathrm{ms}$ long energy pulse of $90\,\mathrm{J\,cm^{-2}}$, at a temperature of $375\,^\circ\mathrm{C}$. The XFAB $180\,\mathrm{nm}$ MOSFET characteristics prior and after the ferroelectric device integration were compared and did not show significant changes [9]. These preliminary results represent a first milestone towards the evaluation of two- and three-terminal synaptic weights based on ferroelectric hafnia using the TEXEL neuromorphic processor.
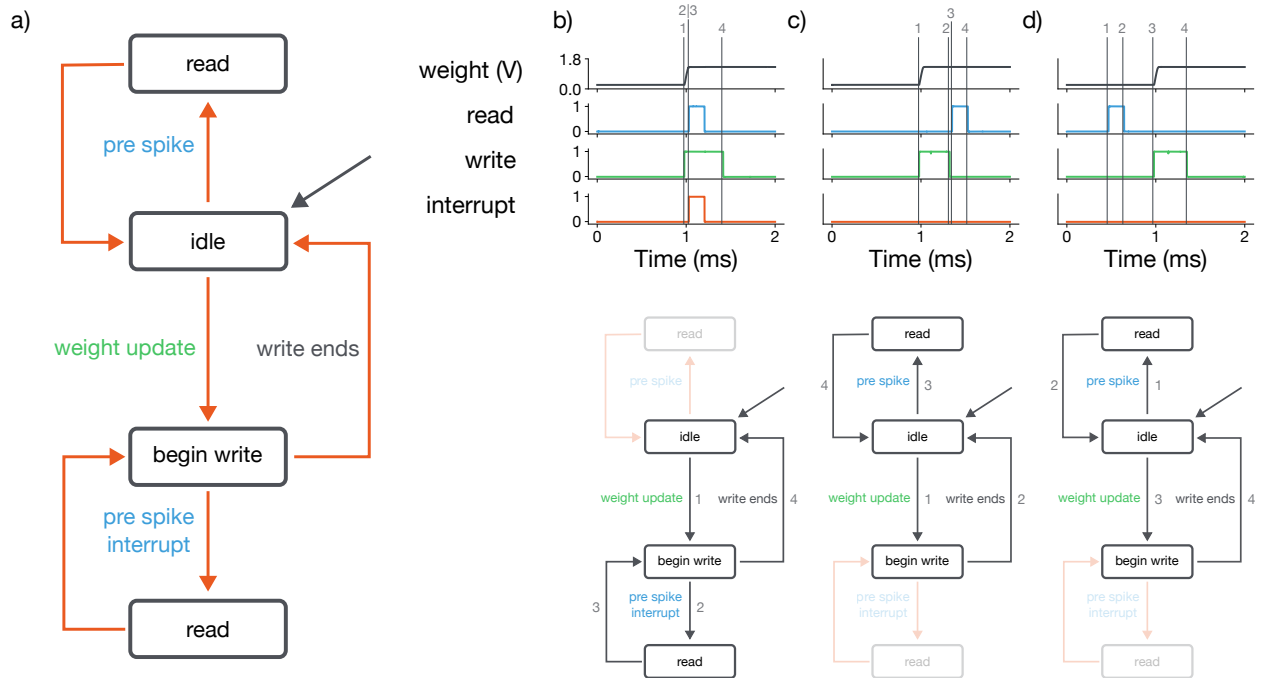
Fig. S2: **Device synapse controller state machine and silicon measurements of the digital flags. a)** A state diagram delineating the internal states of the digital logic governing the addressing protocol for devices on TEXEL. Each row represents a potential combination of presynaptic spikes, postsynaptic spikes, and the state update of synaptic weights. When a presynaptic spike is present, the synaptic weight is read. If a weight update is triggered by either a pre or postsynaptic spike, the logic initiates the writing protocol for the differential device setup. The sequence of these events is unproblematic unless a write and read request are concurrently issued. In such a scenario, a read request takes precedence, and any write request is temporarily halted to allow for the read to take place. Following the reading of the devices, the write process is subsequently executed. **b)** Silicon measurements of digital flags raised by the device controller circuitry located within each synapse. A device read occurs at the same time as a device read, in this case an interrupt flag is raised such that a read can be prioritised and write is subsequently executed. **c)** A write occurs, due to a synaptic weight change, and a read follows. No interrupt flag is raised. **d)** A read, due to a presynaptic spike, occurs before a write. No interrupt flag is raised.

406um x 434um

7.28um

S

PX   CTL   LVL TR NO U ST   W

SY
AHP
IF
PL
PX
D

Abbreviation	Name	Area %
	Synapse	
S	Synapse	-
PX	Pulse Extender	5.4
CTL	Device Controller	31.5
LVL	1.8-5V Level Shifters	5.8
TR	Device Interface	9.9
NO	Normalizer	6
U	Post Synaptic Current	2.2
ST	Synaptic Trace	10.6
W	Bistable Weight/Update Logic	4
	Soma	
SY	PSC Filter	0.4
AHP	Spike Frequency Adaptation	0.34
IF	Leaky Integrate and Fire	
PL	Post Learning Traces	0.43
D	Neuron Digital Logic	0.41
	Wiring and Power	23.02

(a) Neuron block footprint

(b) Key

Fig. S3: The neuron block macro of TEXEL, detailing the location and footprint area of the circuits. a) The footprint of the neuron block with associated labels and sizings. **b)** Table defining the abbreviations and providing the % of area of the neuron block macro they occupy.

■ Plastic high weight
■ Non-plastic
□ Plastic low weight
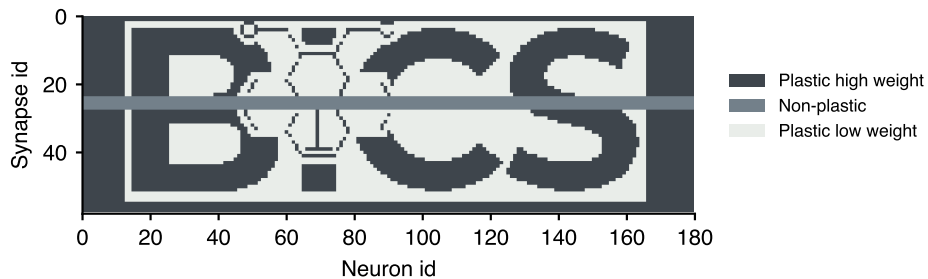
Fig. S4: Readout of a weights matrix programmed onto the plastic synapses of TEXEL. Each of the 54 plastic synapses has the capability to exist in either a high or low state, effectively storing binary information. A weights matrix can be programmed onto the chip, making it suitable for inference tasks, device operation, and testing; independent of on-chip learning.

Supplementary References

[1] E. Voulgari, M. Noy, F. Anghinolfi, F. Krummenacher, and M. Kayal, "Sub-picoampere, 7-decade current to frequency converter for current sensing", in *2015 IEEE 13th International New Circuits and Systems Conference (NEWCAS)*, 2015, pp. 1–4. DOI: 10.1109/NEWCAS.2015.7182071.

[2] F. Corradi and G. Indiveri, "A neuromorphic event-based neural recording system for smart brain-machine-interfaces", *Biomedical Circuits and Systems, IEEE Transactions on*, vol. 9, no. 5, pp. 699–709, 2015. DOI: 10.1109/TBCAS.2015.2479256.

[3] N. Qiao and G. Indiveri, "An auto-scaling wide dynamic range current to frequency converter for real-time monitoring of signals in neuromorphic systems", in *2016 IEEE Biomedical Circuits and Systems Conference (BioCAS)*, 2016, pp. 160–163. DOI: 10.1109/BioCAS.2016.7833756.

[4] B. V. Benjamin, R. L. Smith, and K. A. Boahen, "A low thermal sensitivity subthreshold-current to pulse-frequency converter for neuromorphic chips", *IEEE Journal on Emerging and Selected Topics in Circuits and Systems*, vol. 13, no. 4, pp. 956–964, 2023. DOI: 10.1109/JETCAS.2023.3321105.

[5] T. Delbrück and A. V. Schaik, "Bias current generators with wide dynamic range", *Analog Integrated Circuits and Signal Processing*, vol. 43, no. 3, pp. 247–268, 2005. DOI: 10.1007/s10470-005-1606-1.

[6] M. Ziegler, C. Wenger, E. Chicca, and H. Kohlstedt, "Tutorial: Concepts for closely mimicking biological learning with memristive devices: Principles to emulate cellular forms of learning", *Journal of Applied Physics*, vol. 124, no. 15, p. 152 003, 2018. DOI: 10.1063/1.5042040.

[7] S. Park, B. Spetzler, T. Ivan, and M. Ziegler, "Multilayer redox-based HfOx/Al2O3/TiO2 memristive structures for neuromorphic computing", *Scientific Reports*, vol. 12, p. 18 266, 2022. DOI: 10.1038/s41598-022-22907-5.

[8] M. Hansen *et al.*, "A double barrier memristive device", *Scientific Reports*, vol. 5, p. 13 753, 2015. DOI: 10.1038/srep13753.

[9] L. Bégon-Lours *et al.*, "Back-end-of-line integration of synaptic weights using HfO2/ZrO2 nanolaminates", *Advanced Electronic Materials*, p. 2 300 649, 2024. DOI: 10.1002/aelm.202300649.

[10] R. Hamming-Green, M. S. Ram, D. F. Falcone, B. Noheda, B. J. Offrein, and L. Bégon-Lours, "Multi-level, low-voltage programming of ferroelectric HfO2/ZrO2 nanolaminates integrated in the back-end-of-line", in *2024 8th IEEE Electron Devices Technology & Manufacturing Conference (EDTM)*, IEEE, 2024, pp. 1–3. DOI: 10.1109/EDTM58488.2024.10511719.